

TABLE OF CONTENTS

	Page
INTRODUCTION	1
CHAPTER 1 LITERATURE REVIEW	5
1.1 Anatomy of the heart	5
1.1.1 Cardiac cycle.....	7
1.1.2 Coronary arteries structure.....	8
1.1.3 Electrocardiography (ECG)	9
1.2 Angiography technique in medical imaging.....	11
1.3 Coronary artery disease (CAD)	12
1.3.1 Single axis rotational coronary angiography	13
1.3.2 Dual-axis rotational coronary angiography	14
1.4 Fan-beam computed tomography	16
1.5 Cone-beam computed tomography	17
1.6 Summary of reviews	19
1.7 Hypotheses and Objectives	21
CHAPTER 2 METHODOLOGY	23
2.1 Optimal working view with dual-axis rotational angiography	23
2.1.1 Rate of foreshortening.....	24
2.1.2 Rate of overlapping.....	26
2.1.3 Determination of the optimal working view	27
2.2 Tomographic geometry	28
2.2.1 Cone beam acquisition geometry.....	28
2.2.2 Projection matrix.....	30
2.3 3D CT reconstruction.....	33
2.3.1 Fourier transform	33
2.3.2 Filtered Back-projection	34
2.3.2.1 Filtering.....	34
2.3.2.2 Back-projection.....	37
2.3.3 Cone beam reconstruction process.....	40
2.3.4 FDK algorithm.....	41
2.3.5 ECG-gated in FDK algorithm	42
CHAPTER 3 EXPERIMENTS AND RESULTS.....	47
3.1 Experiment setup	47

3.2 Evaluation and result.....	50
CONCLUSION.....	61
BIBLIOGRAPHY.....	63

LIST OF TABLES

	Page
Table 1.1	Nomenclature for angiography 11
Table 1.2	Comparative analysis of several angiographic techniques 16
Table 1.3	Recent studies about 3D reconstruction of coronary artery..... 20
Table 3.1	The physical characteristics of patients 48
Table 3.2	Rate of overlapping between two branches in different gantry orientations 52
Table 3.3	The quality of the 3D reconstruction for patient-1 in different gantry orientations..... 55
Table 3.4	The quality of the 3D reconstruction for each patient with cardiac motion (when comparing with ground true) 57
Table 3.5	The relation between quality of 3D reconstruction and the heart phase of patient-1 58
Table 3.6	The relation between quality of 3D reconstruction and the gating function window of patient-1 59

LIST OF FIGURES

	Page
Figure 0.1	Quantification of lesion length and percentage stenosis in a 3D reconstruction..... 2
Figure 0.2	Vessel overlap and foreshortening in X-ray image 3
Figure 1.1	Anatomy of the heart 5
Figure 1.2	The cardiac cycle 7
Figure 1.3	Structure of coronary artery in the heart..... 9
Figure 1.4	ECG signal..... 10
Figure 1.5	A sample of coronary angiogram frame 12
Figure 1.6	A normal artery and an artery with plaque buildup..... 13
Figure 1.7	Single axis rotational X-ray angiography in CHU Sainte-Justine..... 14
Figure 1.8	Dual axis rotational X-ray angiography in CHU Sainte-Justine 15
Figure 1.9	Fan beam computed tomography 17
Figure 1.10	Cone beam computed tomography 18
Figure 1.11	Main hypotheses and related objectives 22
Figure 2.1	Positions of patient and gantry 24
Figure 2.2	Foreshortening of coronary artery 25
Figure 2.3	Overlapping between two vessel segments 26
Figure 2.4	Determination of the optimal working view 27
Figure 2.5	Optimal view maps of DARA 28
Figure 2.6	Depiction of CT acquisition geometries..... 30
Figure 2.7	Ramp Filter 35

Figure 2.8	Ramp filtering example	36
Figure 2.9	Sinogram.....	37
Figure 2.10	The Filtered back-projection process	39
Figure 2.11	Cone beam CT reconstruction process.....	40
Figure 2.12	The coordinate system.....	42
Figure 2.13	Prospective ECG triggering.....	43
Figure 2.14	Retrospective ECG Gating	44
Figure 3.1	The acquisition time	47
Figure 3.2	Three datasets generated from XCAT phantom.....	49
Figure 3.3	The motion phase signal.....	50
Figure 3.4	The overlap area between the left anterior descending artery and the circumflex in different gantry orientations	51
Figure 3.5	Extracting centerlines for the projection image with ($\theta = 45^\circ$, $\varphi = 0^\circ$)	51
Figure 3.6	The Dice similarity coefficient.....	53
Figure 3.7	The quality measure of f at the projection image 25 of patient 1.....	54
Figure 3.8	The quality measure of f at each projection image of patient-1	54
Figure 3.9	3D reconstruction of coronary artery using FDK.....	56
Figure 3.9	3D reconstruction of coronary artery using FDK (cont.)	57

LIST OF ABBREVIATIONS

2D	Two Dimensions
3D	Three Dimensions
4D	Three Dimensions Temporal
CT	Computed Tomography
CVD	Cardio-vascular disease
LMCA	Left main coronary artery
LCA	Left main coronary artery
RCA	Right coronary artery
CAD	Coronary artery disease
SCA	Standard Coronary Angiography
SRA	Single-axis Rotational Coronary Angiography
DARA	Dual-axis Rotational Angiography
LAO	Left Anterior Oblique
RAO	Right Anterior Oblique
FDK	Feldkamp Davis Kress
ECG	Electrocardiography
FBT	Filtered Back-projection
PCI	Percutaneous Coronary Interventions

INTRODUCTION

According to the American Heart Association Statistics Committee, Cardio-vascular disease (CVD) is responsible for more than one-third (36.3%) of total deaths in the United States in 2016 (Heart disease and stroke statistics, 2016). In most cases of heart failure, coronary artery lesions are a major factor in the treatment and diagnostic of CVD. Hence, imaging of coronary artery is widely studied.

Currently, clinical assessment relies on direct analysis of X-ray coronary angiographies acquired from several static acquisitions from distinct viewing angles. However, quantitative properties of the vessels such as length, cross-sectional area and orientation cannot precisely be retrieved from the two-dimensional projections. In this context, three-dimensional reconstruction of coronary arteries would be of great clinical interest as it would provide physicians with reliable measures in 3D. In the other hand, a 3D/4D model of the coronary artery provides geometrical and topological information that is necessary to compute the optimal orientation of the imager for stenosis characterization (Minghua Li et al., 2013) or to give an initial point to the computation of the deformation field of the vessels along the cardiac cycle (Taewoo P. et al., 2017).

However, motion blurring induced by the heart beating often degrades cardiac images. Motion artifacts in the coronary artery regions can make analysis harder or, in severe cases, impossible. Due to this reason, the quality of 3D/4D model of coronary artery is impaired, and hence, it reduces the effectiveness in the treatment of CVD.

Some years ago, there were no computerized tools for surgical planning. The surgeons developed the surgical plan based on x-ray images of the patient's heart. The plans were drawn by hand to show the surgical details. This planning method was not precise. Nowadays, a computer-aided system can help the surgeons to perform surgery planning. It can construct 3D coronary model from patient's X-ray images, and visualize it in the computer monitor. It can simulate the surgical plans under the direction of the surgeons. It can also shows the expected surgical result and allow the surgeons to evaluate the results to

determine the best plan. Such as, from the coronary artery structure in simulation the surgeons can know the location of each vessel of coronary artery before performing surgery.

More importantly, the 3D coronary reconstruction can be used in the assessment of the stenosis and lesion in order to find the exact treatments for patients. In the past few years, the treatment depends on the interpretation of the doctors on the 2D x-ray projection images. Therefore, misinterpreted information from the 2D projection may lead to wrong estimation of lesion severity and the wrong choice of stent size. Therefore, it can cause restenosis, thrombosis and increased treatment costs. In order to overcome these diagnostic problems, the quantitative coronary angiography procedure is commonly used (Jin B.L. et al., 2012). With the development of 3D coronary artery reconstruction algorithms, the quantitative coronary angiography can now be performed in the 3D model of coronary artery. As shown in Figure 0.1, the graph shows values of cross-sectional area and the stenosis percentage of the artery along the left anterior descending (LAD) on the 3D coronary artery model of the left side.

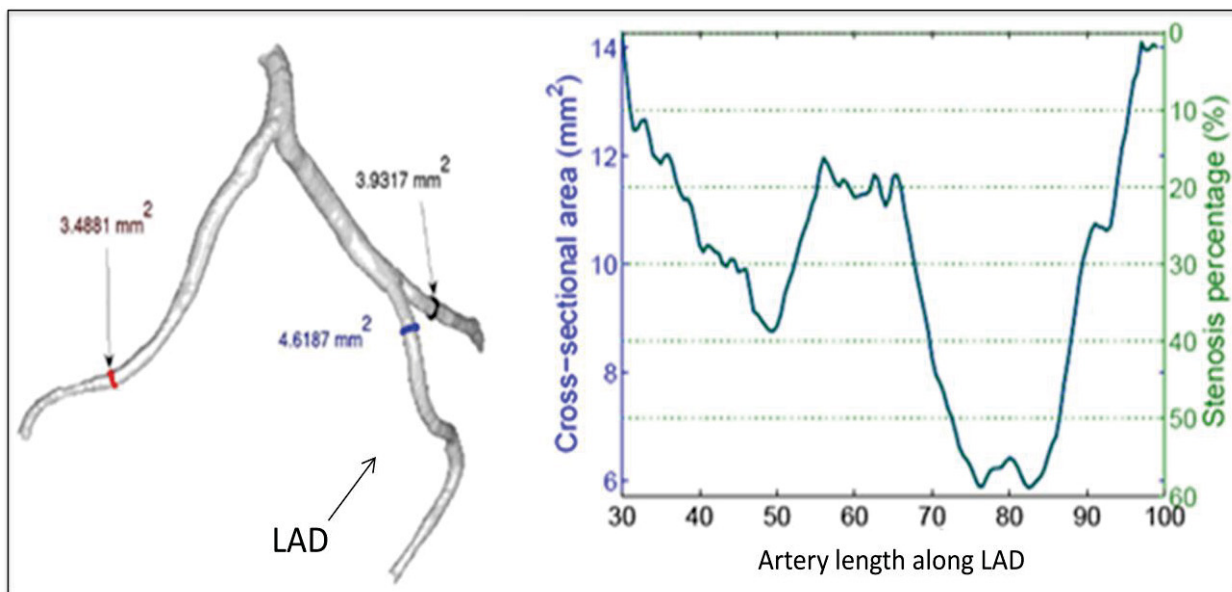


Figure 0.1 Quantification of the stenosis percentage in a 3D reconstruction of coronary artery.

Taken From: <https://na-mic.org/wiki/Projects:BloodVesselSegmentation>

However, there are a few difficulties in 3D/4D reconstruction of the coronary artery. Most of imaging inaccuracies and misrepresentations are related to vessel overlap, and foreshortening. As shown in Figure 0.2, the black circle denotes the origin of the posterior descending artery, and other arrows shows all branches of the right coronary artery. It can be seen that, the body of the right coronary artery is foreshortened and the branch *a* (denotes by black arrow) overlaps the branch *b* (white circle). Overlap results from the superimposed image of one vessel on another. Foreshortening results from the relationship of a vessel segment's longitudinal path with the path of the X-ray beam. This can result in a projection image that may minimize the true length of a vessel segment as well as a coronary lesion.

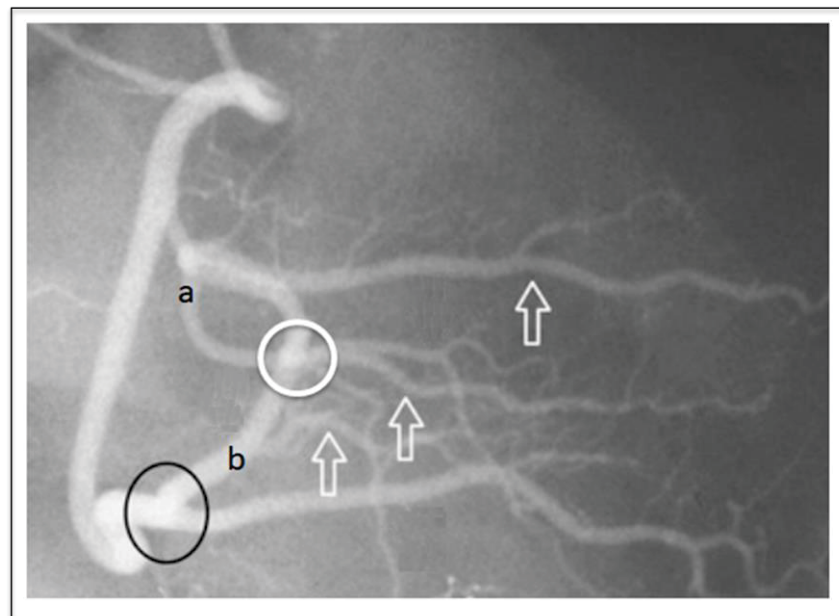


Figure 0.2 Vessel overlap and foreshortening in X-ray image.

The main difficulties that arise for the 3D/4D reconstruction of coronary arteries from angiograms are indeed the respiratory and cardiac motions that are visible in the X-ray projection sequence. The reason is the limitation of the technology in its insufficient temporal resolution, which limits the visualization of fast moving parts of the heart. Due to the long acquisition time of several seconds, the heart beat motion and the breathing motion can be occurred and related to image artifacts. Therefore, it is essential to develop algorithms that can cope with both cardiac and respiratory motion.

Despite continuous progress in X-ray angiography systems, X-ray coronary angiography is fundamentally limited by its 2D representation of moving coronary arterial trees, which can negatively impact assessment of coronary artery disease and guidance of percutaneous coronary intervention. With 3D/3D+time information of coronary arteries, it would improve the navigation in the vessel's pathway. Therefore, my research provides the framework to improve 4D navigation guidance in surgery. It could be a good tool for clinicians in coronary artery disease.

CHAPTER 1

LITERATURE REVIEW

1.1 Anatomy of the heart

The heart is located between the lungs in the middle of the chest, behind and slightly to the left of the breastbone (sternum). The heart contains 4 chambers: the right atrium, left atrium, right ventricle, and left ventricle, as shown in Figure 1.1. The atria are smaller than the ventricles and have thinner, less muscular walls than the ventricles. The atria act as receiving chambers for blood, so they are connected to the veins that carry blood to the heart. The ventricles are the larger, stronger pumping chambers that send blood out of the heart. The ventricles are connected to the arteries that carry blood away from the heart.

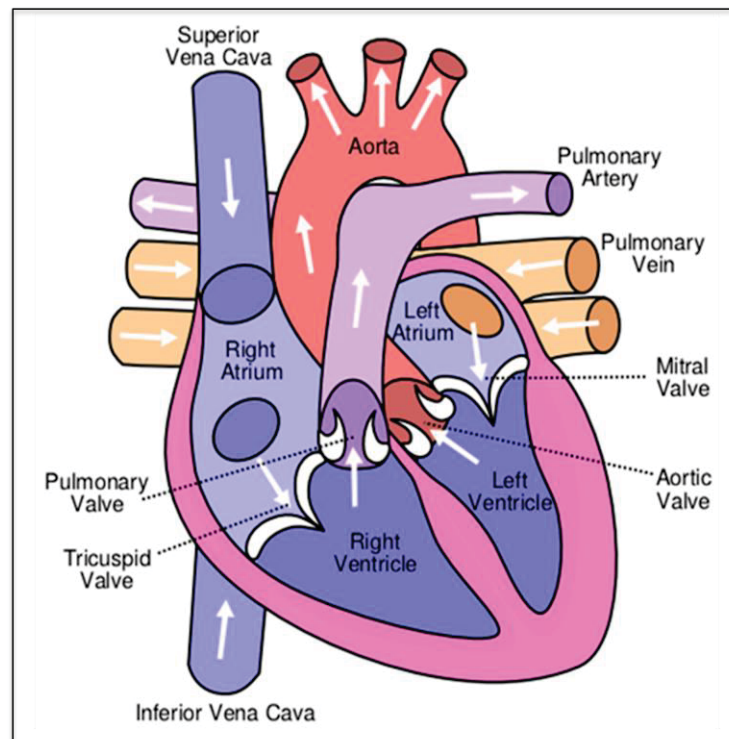


Figure 1.1 Anatomy of the heart.
Taken From: [https://en.wikipedia.org/wiki/
File:Heart_labelled_large.png](https://en.wikipedia.org/wiki/File:Heart_labelled_large.png)

The chambers on the right side of the heart are smaller and have less myocardium in their heart wall when compared to the left side of the heart. This difference in size between the sides of the heart is related to their functions and the size of the 2 circulatory loops. The right side of the heart maintains pulmonary circulation to the nearby lungs while the left side of the heart pumps blood all the way to the extremities of the body in the systemic circulatory loop.

The heart functions by pumping blood both to the lungs and to the systems of the body. To prevent blood from flowing backwards or regurgitating back into the heart, a system of one-way valves are present in the heart. The heart valves can be broken down into two types: atrioventricular and semilunar valves.

- **Atrioventricular valves:** The atrioventricular valves are located in the middle of the heart between the atria and ventricles and only allow blood to flow from the atria into the ventricles. The atrioventricular valve on the right side of the heart is called the tricuspid valve because it is made of three cusps that separate to allow blood to pass through and connect to block regurgitation of blood. The atrioventricular valve on the left side of the heart is called the mitral valve or the bicuspid valve because it has two cusps. The atrioventricular valves are attached on the ventricular side to tough string called chordae tendineae. The chordae tendineae pull on the atrioventricular valves to keep them from folding backwards and allowing blood to regurgitate past them. During the contraction of the ventricles, the atrioventricular valves look like domed parachutes with the chordae tendineae acting as the ropes holding the parachutes taut.
- **Semilunar valves:** The semilunar valves are located between the ventricles and the arteries that carry blood away from the heart. The semilunar valve on the right side of the heart is the pulmonary valve, so named because it prevents the backflow of blood from the pulmonary trunk into the right ventricle. The semilunar valve on the left side of the heart is the aortic valve, named for the fact that it prevents the aorta from regurgitating blood back into the left ventricle. The semilunar valves are smaller than the atrioventricular valves and do not have chordae tendineae to hold them in place. Instead, the cusps of the semilunar valves are cup shaped to catch regurgitating blood and use the blood's pressure to snap shut.

1.1.1 Cardiac cycle

The period of time that begins with contraction of the atria and ends with ventricular relaxation is known as the cardiac cycle. The period of contraction that the heart undergoes while it pumps blood into circulation is called systole. The period of relaxation that occurs as the chambers fill with blood is called diastole (as shown in Figure 1.2). Both the atria and ventricles undergo systole and diastole, and it is essential that these components be carefully regulated and coordinated to ensure blood is pumped efficiently to the body. Therefore, the cardiac cycle includes a description of the systolic and diastolic activities of the atria and ventricles, the blood volume and pressure changes within the heart, and the action of the heart valves.

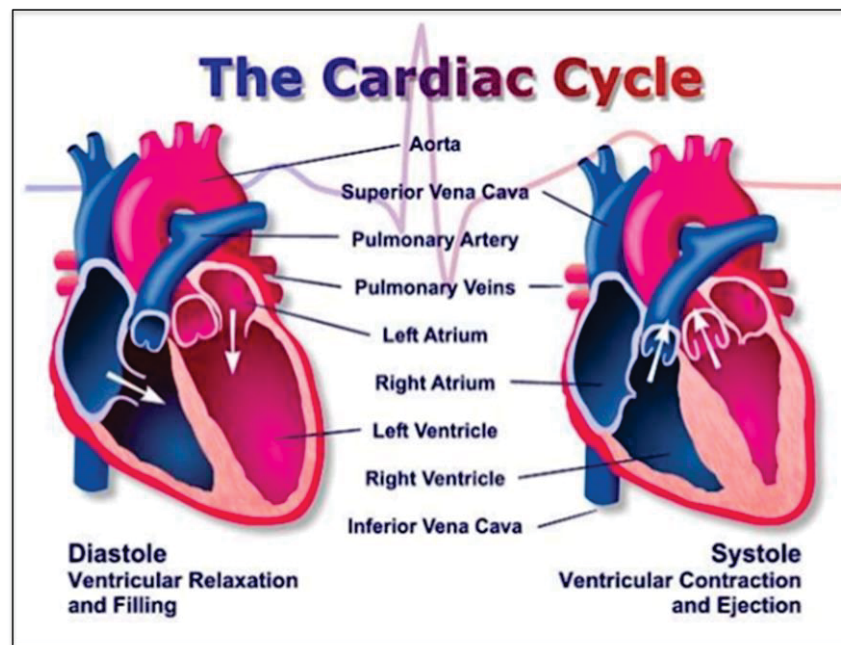


Figure 1.2 The cardiac cycle.

Taken From: https://en.wikipedia.org/wiki/Cardiac_cycle

Diastole represents the period of time when the ventricles are relaxed (not contracting). Throughout most of this period, blood is passively flowing from the left atrium and right atrium into the left ventricle and right ventricle, respectively. The blood flows through atrioventricular valves (mitral and tricuspid) that separate the atria from the ventricles. The right atrium receives venous blood from the body through the superior vena cava and inferior vena cava. The left atrium receives oxygenated blood from lungs through four pulmonary veins that enter the left atrium. At the end of diastole, both atria contract, which propels an additional amount of blood into the ventricles.

Systole represents the time during which the left and right ventricles contract and eject blood into the aorta and pulmonary artery, respectively. During systole, the aortic and pulmonic valves open to permit ejection into the aorta and pulmonary artery. The atrioventricular valves are closed during systole, therefore no blood is entering the ventricles; however, blood continues to enter the atria through the vena cava and pulmonary veins.

1.1.2 Coronary arteries structure

The coronary arteries wrap around the outside of the heart and dive into the heart muscle to bring blood. There are two main coronary arteries (as shown in Figure 1.3): left main and right coronary arteries.

- Left main coronary artery (LMCA): It supplies blood to the left side of the heart muscle. The left main coronary divides into smaller branches:
 - ✓ The left anterior descending artery: branches off the left coronary artery and supplies blood to the front of the left side of the heart.
 - ✓ The circumflex artery: branches off the left coronary artery and encircles the heart muscle. This artery supplies blood to the outer side and back of the heart.
- Right coronary artery (RCA): The right coronary artery divides into smaller branches, including the right posterior descending artery and the acute marginal artery. The right coronary artery supplies blood to the right ventricle, the right atrium of the heart.

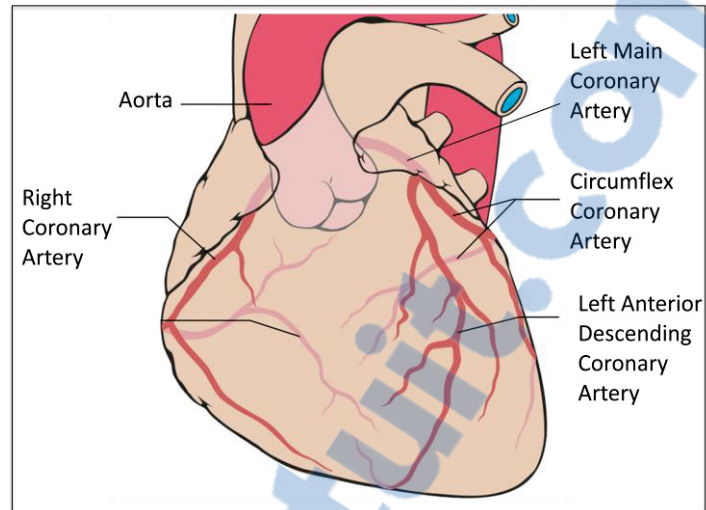


Figure 1.3 Structure of coronary artery in the heart.
 Taken From: https://en.wikipedia.org/wiki/Coronary_circulation

1.1.3 Electrocardiography (ECG)

The electrocardiogram (ECG) records from the body surface and registers the differences in electrical potential generated by the heart. The signal recorded is determined by action potentials generated by millions of individual cells and their sequence of activation. In basically, the electrical system of the heart consists of two types of cells, one for dictating the heartbeat and the other for transmitting this pulse in a precise sequence synchronized with the entire myocardium.

A cardiac cycle starts from the sinus node, which is located on the right atrium wall. The depolarization of the cells, which takes place between 70 and 100 times per minute, has the effect of creating an action potential, which causes a contraction of the heart muscle.

Each cell has its own electrical pulse of varying intensity and direction. Each of these impulses can be represented as millions of vectors. Since the transmission of the pulse follows an ordered sequence, by summing these vectors at certain precise moments of the cardiac cycle, it is possible to extract from there five main vectors each following a precise axis.

Using electrodes placed on the skin of the patient, it is possible to graphically represent his cardiac electrical activity. This study is called electrocardiography and traces in waveform the variations of electrical potential. The waves named P, Q, R, S and T, which emerge from the electrocardiograph, are then the electrical representation of the main vectors. The graph of the waves then allows a three-dimensional representation of the electrical axes of the heart and helps the physician to detect different cardiac pathologies (as shown in Figure 1.4).

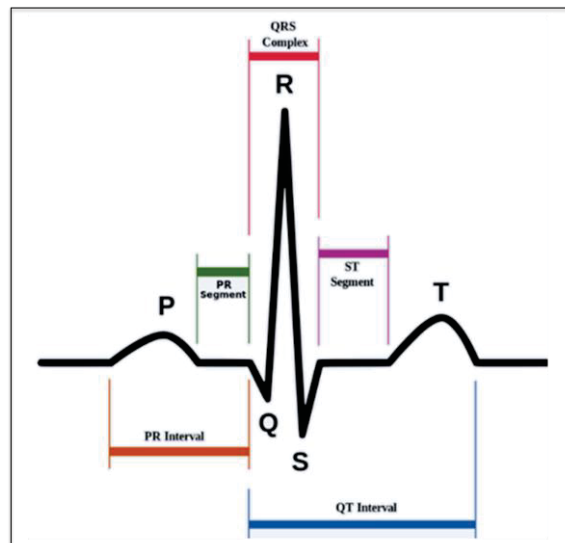


Figure 1.4 ECG signal.
Taken From: <https://en.wikipedia.org/wiki/Electrocardiography>

In the context of motion compensation, the ECG is of great importance since it becomes possible to induce an expected deformation of the coronary arteries as a function of the instant in the cardiac cycle. For example, ventricular systole begins at the beginning of the QRS complex, while the systole of the atrium occurs at the beginning of the P wave. Although the age of the patient and the heart rate has an impact on the duration of the various waves, this information nevertheless allows anticipating the cardiac movements to come.

1.2 Angiography technique in medical imaging

Angiography is a medical imaging technique used to visualize lumen of blood vessels. The technique to visualize blood vessels that supply blood to our heart muscles or coronary arteries is a coronary angiogram. Kenneth et al. reported this technique is the number one modality that used to analyze our vascular system in term of structure and functionality.

The coronary angiogram is an X-ray test where the patient will be injected with contrast dye through the radial or the femoral to show blockage or narrowing inside of the artery. It will give the information of location and the percentage of the blockage or plaque. The information of angiogram can help medical practitioners to determine the suitable treatment for the patient, such as angioplasty or stent or medical therapy. Generally, experts interpret and analyze the image based on their experience.

A 2D image taken by the monoplane C-arm system shows the heart and the angiography from different angles of projection. The nomenclature of angiography projection as stated in (Kern M. L., 2011) is shown in Table 1.1. Figure 1.5 is a sample of a 2D image where the angulation is taken by the monoplane C-arm system shows part of angiography of coronary artery when the contrast media injected into the patient's artery.

Table 1.1 Nomenclature for angiography

Angulation	Definition
Anteroposterior (AP) position	The image intensifier is directly over the patient with the beam traveling perpendicularly back to front (i.e., from posterior to anterior) to the patient lying flat on the x-ray table.
RAO position	The image intensifier is on the right side of the patient (A, anterior; O, oblique).
LAO position	The image intensifier is on the left side of the patient.
Cranial	The image intensifier is tilted toward the head of the patient.
Caudal	The image intensifier is tilted toward the feet of the patient.

Previous works in (Jin Bae Lee et al., 2012) emphasized that coronary angiograms depicts the coronary artery lumen in 2D silhouette. It can be used for quantitative measurement of cardiovascular disease and the progress. Follow the gold standard of the coronary angiograms technique, tremendous works had been made, especially in segmentation and 3D reconstruction of the coronary vessel tree based on the modality to facilitate medical field such as works by (Andriotis A. *et al.*, 2008).

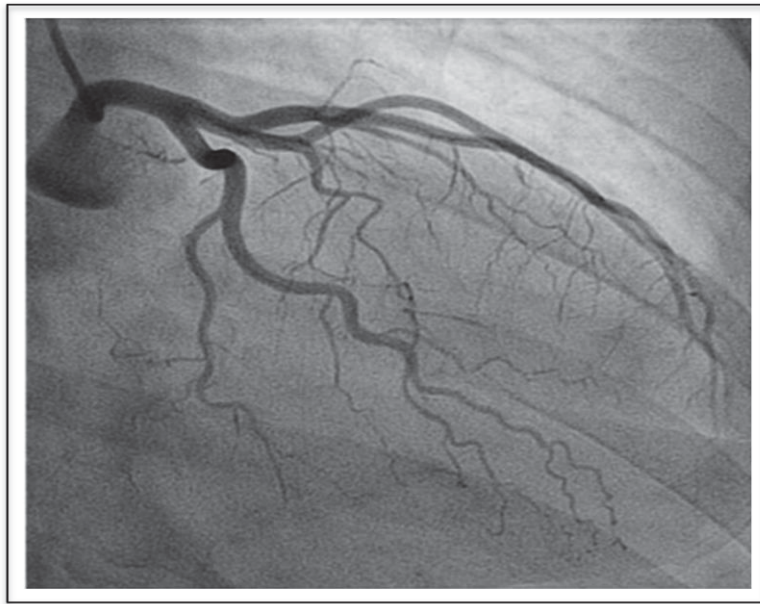


Figure 1.5 A sample of coronary angiogram frame.
Taken at CHU Sainte-Justine.

1.3 Coronary artery disease (CAD)

As mentioned in the previous section, coronary arteries deliver blood to the heart muscle, any coronary artery disorder or disease can have serious implications by reducing the flow of oxygen and nutrients to the heart muscle. This can lead to a heart attack and possibly death. Hence, CAD is the main reason for cardiovascular disease becomes the leading cause of death in worldwide. Figure 1.6 shows a segment of normal artery with normal blood flow and also one narrowing of the artery with the corresponding cross-sectional view.

In cases of severe coronary artery stenosis, clinicians may have to perform coronary bypass surgery using image-guided robotic surgical systems. However, the restricted field of view of the stereo endoscopic images makes the vessel mis-identification and mis-localization (Anwar A. et al., 2013). Moreover, motion of the heart and respiratory motion are also important causes of making this treatment more difficult. Therefore, the main purpose of this project is to solve those problems.

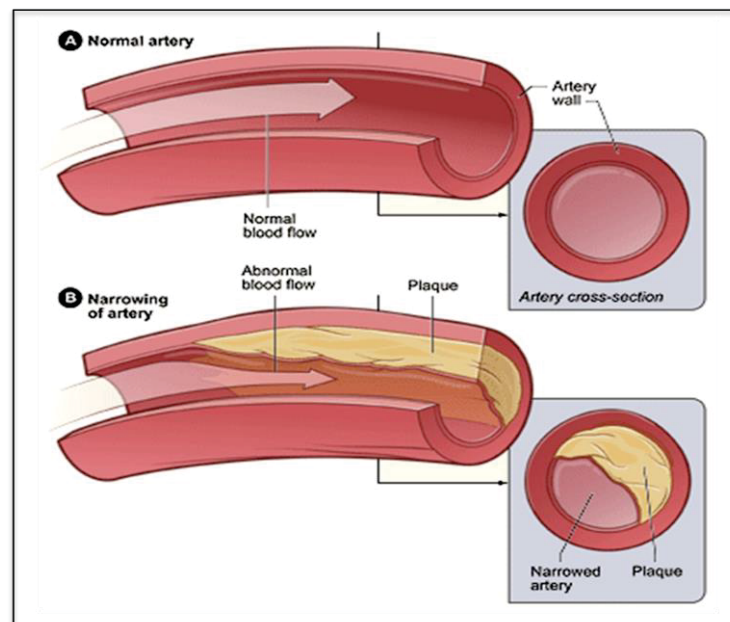


Figure 1.6 A normal artery and an artery with plaque buildup.

Taken From: <https://en.wikipedia.org/wiki/Heart>

1.3.1 Single axis rotational coronary angiography

Although conventional coronary angiography has been improved considerably during the past 20 years such as the quality of the image, post-processing enhancement, high quality screen displaying, and tools for playback and the quantification of the lesion, it still has limitations inherent to 2D images of the translucent inner diameter, lumen, coronary arteries, and the clear risk of exposure to radiation and contrast media. These restrictions have led to the need for alternative technology allows for more precise characteristics of the vessel of coronary arteries, lesions, and stents.

Single axis rotational angiography is a new image acquisition technique, which was developed recently to address some the limitations of the traditional angiography technique (Garcia *et al.*, 2007), as shown in Figure 1.7. It acquires the same images as traditional angiography but is automated, can be standardized, and provides an extensive panoramic view of key anatomic features for diagnostic and interventional purposes.



Figure 1.7 Single axis rotational X-ray angiography in CHU Sainte-Justine.

1.3.2 Dual-axis rotational coronary angiography

Dual-axis rotational coronary angiography (in Figure 1.8) is an improved form of the single axis rotational angiography. The most important difference is that it can be moved two gantry hands simultaneously in two directions, left anterior oblique (LAO) to right anterior oblique (RAO) and cranial to caudal, as shown in Figure 2.1. Hence, this technological advancement can obtain numerous unique images of the left or right coronary tree with a single coronary injection.



Figure 1.8 Dual axis rotational X-ray angiography in CHU Sainte-Justine.

The conventional coronary angiography technique uses the radiographic contrast to display a two dimensional silhouette of a vessel's three dimensional structure. Basically, 2D images only display certain vessel characteristics, and hence, the combination of vessel tortuosity, overlap, suboptimal projections, and individual anatomic variation may result in insufficient 2D images and may partially account for the suboptimal sensitivity of coronary angiography. With the addition of cranial and caudal angulation to standard oblique views, DARA can improve visualization and led to the recognition that an optimal view existed for most vessel segments which allows a projection with the least amount of radiographic vessel foreshortening and radiographic vessel overlap (Hudson *et al.*, 2010).

On the other hand, this innovative technology demonstrates significant potential in enhancing the number of angiographic projections obtainable with superior imaging results while reducing safety concerns related to contrast volume and radiation exposure as shown in Table 1.2.

Table 1.2 Comparative analysis of several angiographic techniques

	CA	SRA	DARCA
Contrast volume	least favorable	most favorable	most favorable
Radiation exposure	least favorable	most favorable	most favorable
Procedural time	normal	normal	least favorable
Image content	least favorable	normal	most favorable
Ease of use	most favorable	normal	Normal

1.4 Fan-beam computed tomography

In X-ray CT scans, fan beam imagery is a quite common approach to the projection geometry implementation (Zeng *et al.*, 2010). The x-ray focal point is displayed as the “X-ray source” in Figure 1.9, angling out to create a fan shape before hitting the sensors at the detector array of the opposite side. The patient is imaged slice-by-slice, usually in the axial plane, and interpretation of the images is achieved by stacking the slices to obtain multiple 2D representations. Data is gathered using the narrow fan beam, slightly changing the angle of the x-ray source to collect data from many slices. After data is collected, the image slices are then compiled to create two dimensional representations of parts of the object. The linear array of detector elements used in conventional helical fan-beam CT scanners is actually a multi-detector array. This configuration allows multi-detector CT scanners to acquire up to 64 slices simultaneously, considerably reducing the scanning time compared with single-slice systems and allowing generation of 3D images at substantially lower doses of radiation than single detector fan-beam CT arrays.

Advantages of fan beam CT include:

- Greater soft tissue definition (the difference in soft tissue resolution is shown in the scans on the left).
- Greater bone resolution.

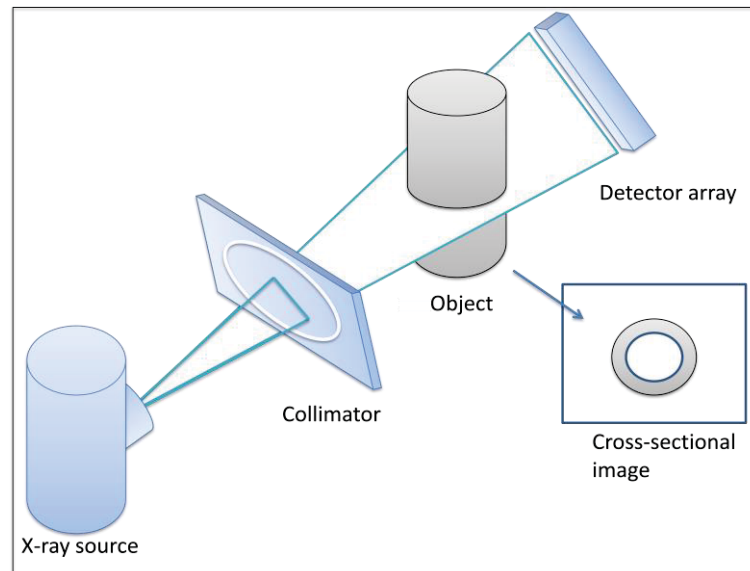


Figure 1.9 Fan beam computed tomography.

However, a disadvantage of fan beam imaging is that part of the image data may be truncated due to the limited field of view from the magnification factor, causing spikes and other artifacts around the edges of the image (Min Y. et al., 2017).

1.5 Cone-beam computed tomography

Cone-beam CT scanners, on the other hand, are based on volumetric tomography, using a 2D extended digital array providing an area detector. The cone-beam geometry immediately captures a 2D image through a 3D x-ray beam, which scans in the shape of a cone. The cone-beam technique involves a single 360° scan in which the x-ray source and a reciprocating area detector synchronously move around the object of interest, as displayed in Figure 1.10. This three dimensional beam proves efficient as at most one rotation around the object provides enough information to reconstruct a three dimensional image (Sedentext, 2016). At certain degree intervals, single projection images, known as “basis” images, are acquired.

These are similar to lateral cephalometric radiographic images, each slightly offset from one another. This series of basis projection images is referred to as the projection data. Software program incorporating sophisticated algorithms including back-filtered projection are applied

to these image data to generate a 3D volumetric data set, which can be used to provide primary reconstruction images in 3 orthogonal planes (axial, sagittal and coronal).

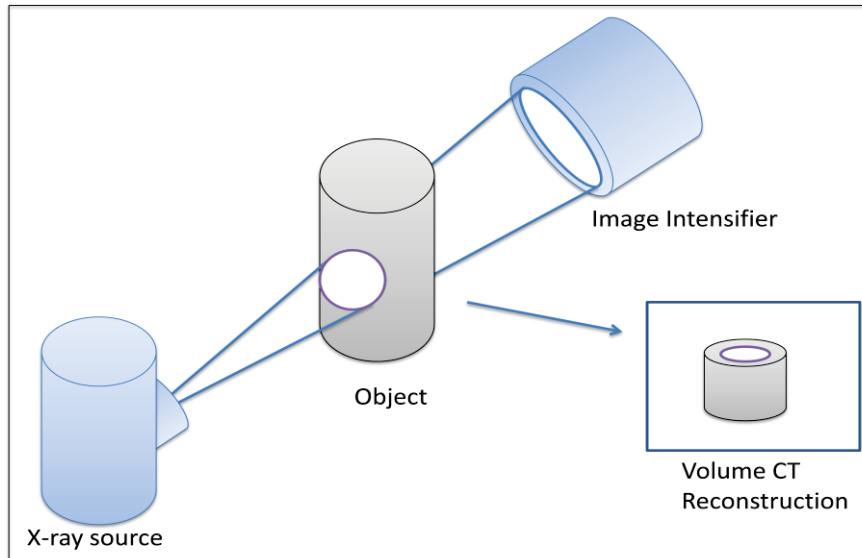


Figure 1.10 Cone beam computed tomography.

The rapid acquisition of information causes cone-beam projections to be more favourable than fan-beam projections due to the shorter procedure time and therefore less possibility of quality loss due to patient movement (Scarfe et al., 2008). The shorter procedure time also limits the patient's exposure to radiation. The ability to capture two dimensional images in a single attempt provides higher quality images than the fan-beam X-ray geometry.

Moreover, the cone beam CT includes other advantages:

- Lower radiation dosage.
- Lower cost.
- Less artifacts with metallic objects.
- Available for mobile 3D C-arm.

1.6 Summary of reviews

The current literature review allowed us to discuss the usual techniques proposed in the literature to solve several problems related to the 3D reconstruction of the coronary arteries from an angiographic sequence.

Most 3D reconstruction methods are semi-automatic, requiring manual input such as the deformable curve (Yang J. et al., 2014) to extract vessel centerlines. This method need to be inputted two frontier points and two posterior points by the user. Fully automatic methods are generally more demanding in terms of computation time and offer lower quality results. Several approaches using the 2D coronary artery branches tracking have been proposed by Cimen S. et al. (2014). A major problem with this type of method is the difficulty of performing a perfect tracking when there is overlap. The second most common category of reconstruction methods is point-to-point correspondence with energy minimization. Based on the projective geometry, it is possible to quickly determine point-to-point correspondences from one view to another of a sequence as proposed by Mufit Cetin, Ali Iskurt (2016). Despite the potential use in an interventional context, this method offers mixed results when segments are parallel to the epipolar lines. In addition, if segments are close together in the 2D images or the segmentation is not perfect, the matched points may contain discontinuities. Table 1.3 presents the different 3D reconstruction methods of the literature. They are categorized and presented the advantages and disadvantages of each. It is thus noticed that none of the methods presented is robust, automatic, and rapid execution for the interventional context.

Table 1.3 Recent studies about 3D reconstruction of coronary artery

Article	Methods	Advantages / Disadvantage
Cristiano B. et al., (2015)	<p>+ They used the combination of intravascular ultrasound and angiography.</p> <p>+ For geometrical characterization purposes, tridimensional center lines were obtained. Three vessels were reconstructed : two left anterior descending arteries and one left circumflex artery.</p>	<p>Advantage : This method increases the practicality of the reconstruction with a gain in volumetric accuracy of the vessel.</p> <p>Disadvantage : It makes a more complex initialization task.</p>
Cimen S. et al., (2014)	<p>+ A synthetic rotational data using the single left coronary artery geometry of the 4D Xcat phantom.</p> <p>+ This study uses a statistical bilinear model of ventricular epicardium as spatio-temporal model. The 3D+t reconstruction performance of this algorithm is stable even under 1.25mm 2D observation noise.</p>	<p>Advantage : This method is stable and it is able to handle missing data.</p> <p>Disadvantage : There are some outliers in results.</p>

Table 1.3 Recent studies about 3D reconstruction of coronary artery (cont.)

<p>Mufit Cetin, Ali Iskurt (2016)</p>	<p>+ They used X-ray angiography and CT for their research.</p> <p>+ To extract the bifurcation points, they used an automatic and novel pattern recognition technique. Then they applied a novel optimization algorithm for matching the branches.</p> <p>+ The accuracy of the bifurcation extraction is high. Accuracy of vessel centerlines has rms error smaller than 0.57mm.</p>	<p>Advantage: branch by branch reconstruction avoids mismatched and mis-overlapped branches.</p> <p>Disadvantage: They did not try more angiograms with noise perturbations. And viewing angle is still a challenge.</p>
<p>Yang J. et al., (2014)</p>	<p>+ The phantom data were simulated from the CTA data.</p> <p>+ An external force back-projective composition model is developed to determined the external force. Then the deformable curves evolves toward the true vascular center lines in 3D space.</p> <p>+ The coronary arteries hidden can be observed clearly in 3D model.</p>	<p>Advantage : This is a robust method for reconstruction coronary arteries from two monoplane angiographic images.</p> <p>Disadvantage : The reconstruction may fail when larger curvature variances are present.</p>

1.7 Hypotheses and Objectives

The main objective of this study is to provide a framework to address the limitation about overlap and foreshortening between vessels in lesions detection and develops a 3D dynamic reconstruction of coronary artery as well. This research will particularly be focused on helping physicians in the study, treatment and a good guide for interventional cardiac.

To achieve this goal, the dual-axis coronary artery angiography is used to acquire data from the patient to reduce the radiation dose as well as the enhancement quality of 3D reconstruction. The first objective is proposed to provide a method for physician working with the dual-axis coronary angiography technique. This objective is based on the hypothesis in which the dual-axis coronary angiography can be solved the foreshortening effect and the overlapping effect. The second objective is proposed to provide a dynamic reconstruction method for coronary artery. This objective is based on the hypothesis in which the FDK reconstruction algorithm can be compensated the cardiac motion of coronary artery. The main hypotheses and related objectives of this project and the connection among the objectives are illustrated in Figures 1.11.

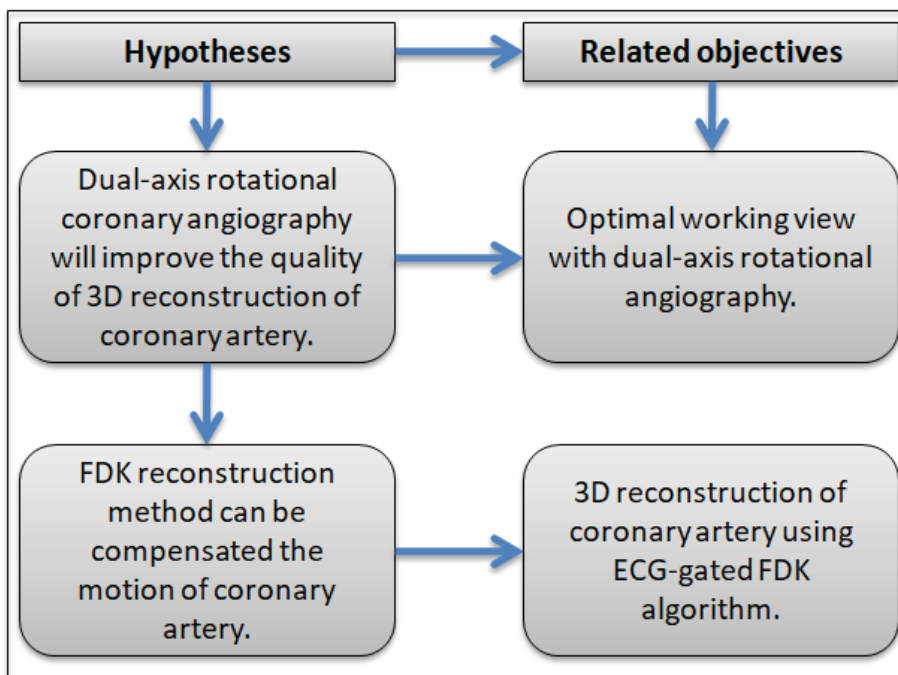


Figure 1.11 Main hypotheses and related objectives.

CHAPTER 2

METHODOLOGY

2.1 Optimal working view with dual-axis rotational angiography

The conventional coronary angiography technique is limited by its two-dimensional (2D) representation of three-dimensional structures. Vessel foreshortening in angiographic images may cause errors in the assessment of lesions or the selection and placement of stents. To address this problem, the dual-axis rotational coronary angiography technique has been introduced, in which the C-arm rotates in two axes during scanning has allowed visualization of the coronary tree by using a single contrast injection. In this technique, rotation angles are used to determine the imaging orientation of the C-arm; these angles are generally defined as the left/right anterior oblique (LAO/RAO) and the caudal/cranial (CAUD/CRAN). In imaging, a physician adjusts these rotation angles to achieve different perspective projections of the coronary arteries. If these angles are incorrect, segments with stenosis are very difficult to be visualized in a 2D angiogram because of foreshortening and overlapping effects. Hence, the first objective is proposed in this section to help physical to choose the optimal working view with the dual-axis rotational angiography technique.

We consider that a dynamic sequence of 3D coronary tree is available by reconstruction of the 3D coronary tree from the projections acquired at each phase of the cardiac cycle and proceed along the following stages to compute the optimum angular position of the C-arm:

- Computation of the foreshortening degree for the segment of interest and its overlapping rate with adjacent segments, for each relevant gantry orientation and cardiac phase.
- Selection of the best angles and result displaying for validation by the cardiologist.

The imaging apparatus consists of an X-ray source and a flat panel detector (or image intensifier) at opposite ends of the C-arm gantry (Figure 2.1). This C-arm machine rotates around the patient. Parameters defining the C-arm geometry are:

- The primary angle θ which represents a rotation of the C-arm along an arc from patient's left to right sides (from left anterior oblique to right anterior oblique view).
- The secondary angle φ , which describes a rotation of the gantry along an arc from the patient's head to feet (Cranial to Caudal).
- The distance from the X-ray source to the iso-center (Source to Object Distance – SOD).
- The distance from the X-ray source to the detector (Source to Image Distance – SID).

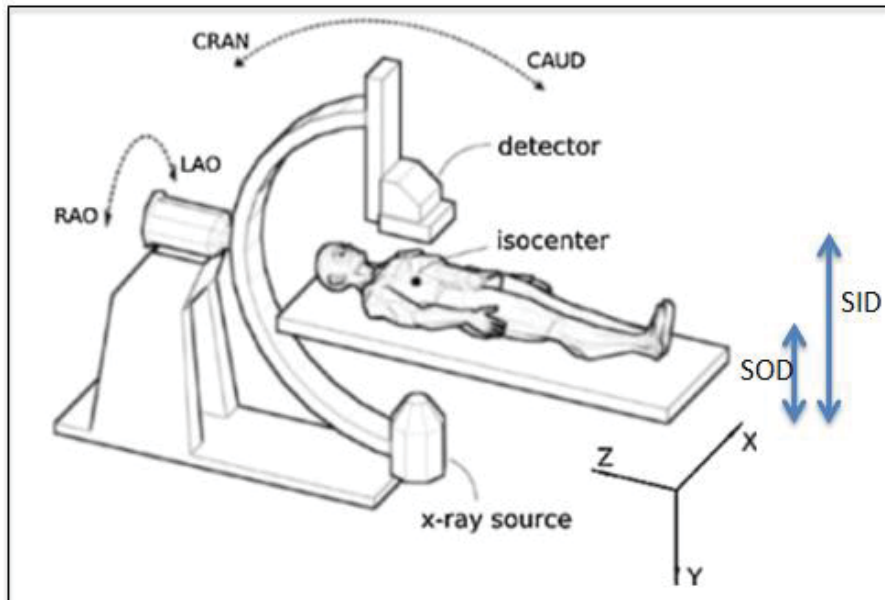


Figure 2.1 Positions of patient and gantry.

2.1.1 Rate of foreshortening

Foreshortening occurred when the propagation direction of X-ray is not perpendicular to the vessel segment, the projection of the vessel in a 2D image is shorter than the actual length in a 3D space. Foreshortening rate is determined on the basis of the length of a vessel segment and the angle between the X-ray propagating direction and the normal vector of the vessel segment. And this angle depends on the two angles of the gantry orientation (θ , φ).

We denote p_n is the location of n^{th} point on the vessel segment S in a cardiac cycle (with $n \in [1, N]$) and P_{θ, φ_j} is the forward projection of the vessel segment according to the orientation of the gantry (θ_i, φ_j) . Foreshortening rate can be defined as follows:

$$f(\theta_i, \varphi_j, S) = \left(1 - \frac{\sum_{n=1}^N (P_{\theta_i, \varphi_j}(p_n) - P_{\theta_i, \varphi_j}(p_{n-1}))}{\max \sum_{n=1}^N (P_{\theta, \varphi}(p_n) - P_{\theta, \varphi}(p_{n-1}))} \right) \quad (2.1)$$

Figure 2.2 shows the projected centerline of the vessel segment is the intersection curve of the X-ray beam and the image plane to describe about this phenomenon with rates of 0% and 20%.

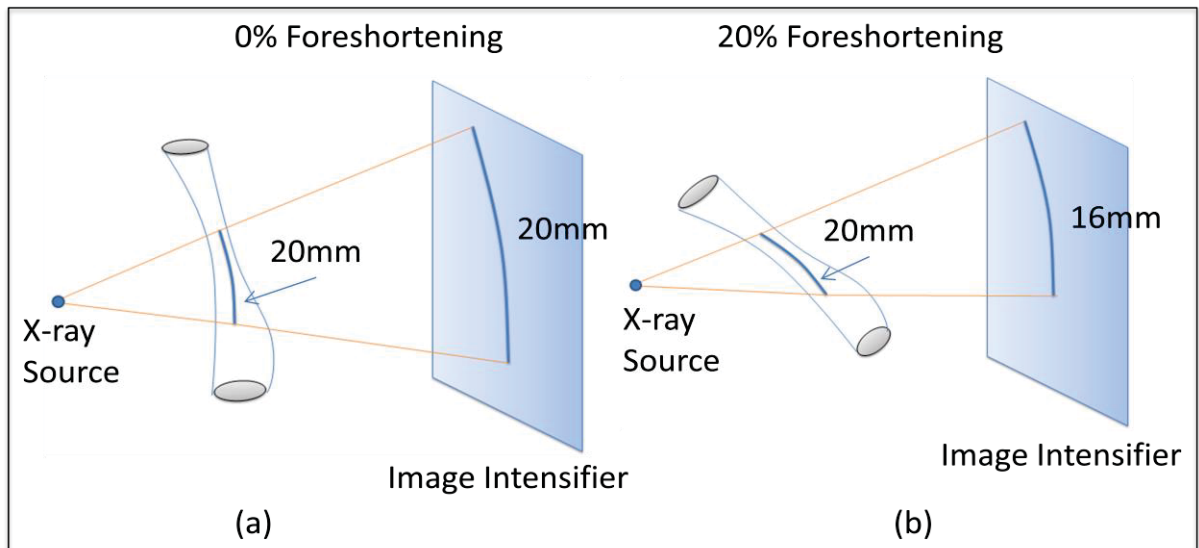


Figure 2.2 Foreshortening of coronary artery: (a) With rate of 0%,
(b) With rate of 20%.

2.1.2 Rate of overlapping

Overlapping indicates that the vasculature in the same direction of the X-ray propagation path may overlap the same image area as shown in Figure 2.3. The optimum viewing angle should exhibit a minimum overlapping rate of the whole vasculatures. For each clinically relevant gantry orientation, the amount of vascular segment overlapping can be expressed by the segment of interest in 2D space (Garcia JA et al., 2009).

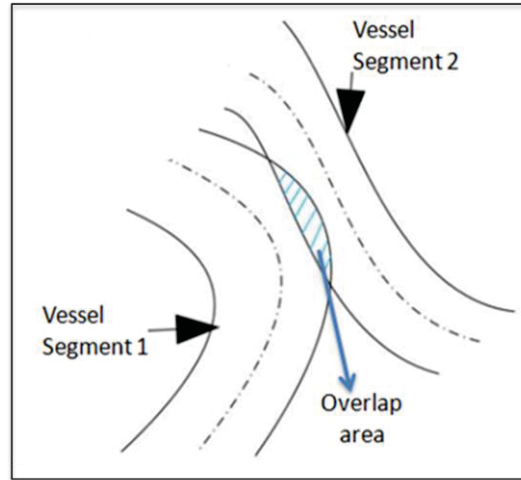


Figure 2.3 Overlapping between two vessel segments.

Let S_i represent the i^{th} sampling area of the vessel segment in the projection image at angle (θ, φ) and S_j represent the j^{th} sampling area of other vessel segments in the projection image at angle (θ, φ) . The overlapping rate can be calculated by counting the pixels in the projected image as below:

$$O(\theta, \varphi) = \left(\frac{\Pi_{\theta, \varphi}(S_j \cap (\bigcup_{i=1, i \neq j}^n S_i))}{\Pi_{\theta, \varphi}(S_j)} \right) \quad (2.2)$$

2.1.3 Determination of the optimal working view

The determination of the optimal working view is performed by combining rate of foreshortening and rate of overlapping. The rate of foreshortening is first computed for all considered pairs of angles (θ, φ) and each cardiac phase. Thus for each couple of angles, we chose the median value over the computed K rates of foreshortening and applied a threshold to select gantry orientations for which the median rate is lower than 10%. The overlapping rate is afterward calculated for each cardiac phase and for each retained orientation. Finally, we can obtain the optimal view in which various vessel segments are foreshortening and overlap with the minimum rate. The steps for selecting the optimal working view are shown in the Figure 2.4.

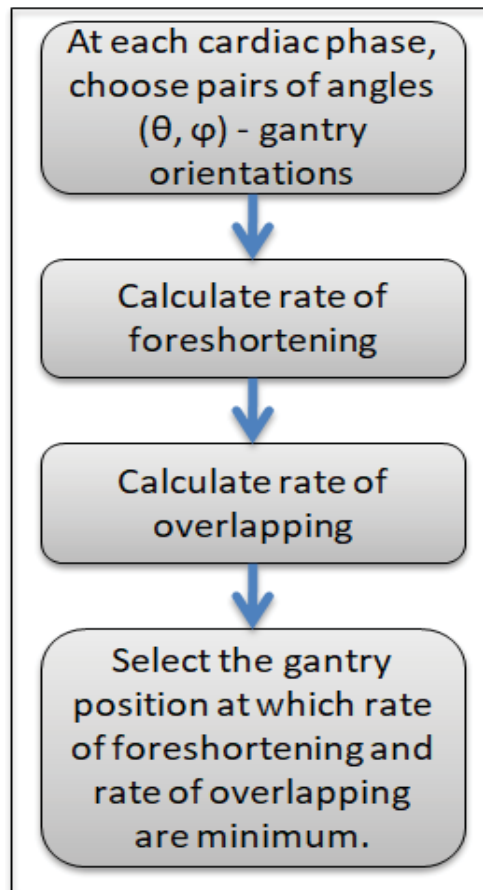


Figure 2.4 Determination of the optimal working view.

Figure 2.5 demonstrates the angiographic projections of DARA in which various coronary segments are optimally visualized with the generation of optimal view maps (Hudson *et al.*, 2010). In this Figure these optimal view maps per vessel segment were generated from 3D reconstruction of coronary artery obtained in a single acquisition with multiple projections. It indicates the greatest to the least amount of vessel foreshortening and overlap. The patient specific optimal view maps are represented by the middle box, and the stenosis is represented by a yellow segment in the left coronary artery tree. As shown in this figure, the stenosis segment is most foreshortened at the red position, and is least foreshortened at the green position.

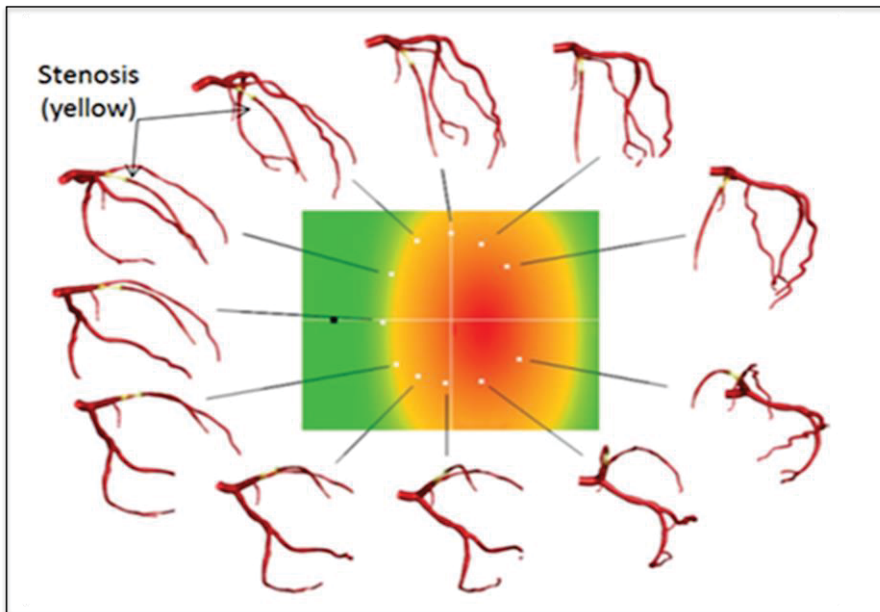


Figure 2.5 Optimal view maps of DARA.
Adapted from Hudson PA et al. (2010).

2.2 Tomographic geometry

2.2.1 Cone beam acquisition geometry

The cone-beam geometry was developed as an alternative to conventional CT using either fan-beam or spiral-scan geometries, to provide more rapid acquisition of a data set of the entire field of view and it uses a comparatively less expensive radiation detector. A divergent pyramidal or cone shaped source of ionizing radiation is directed through the middle of the

area of interest onto an area x-ray detector on the opposite side. The x-ray source and detector rotate around a rotation fulcrum fixed within the center of the region of interest. During the rotation, multiple sequential planar projection images of the field of view are acquired in a complete, or sometimes partial.

We assume that projection data is acquired with the x-ray source point moving along a connected curve $x(\alpha)$ in space, which is called the source trajectory. X-ray measurements give samples of the function g , as shown below.

$$g(\alpha, \beta) = \int_0^{\infty} f(x(\alpha), t\beta) dt \quad (2.3)$$

In equation (2.3), β is used to describe the unit direction of the measurement ray. It corresponds to a general definition of cone beam data and the set of potential realizations of the vector β depends on the geometry of the detector that is used for data acquisition. Values of g is called cone beam data, and cone beam data at fixed α will be referred to a cone beam projection. If all non-zero values of the function g at α fixed are known, the corresponding cone beam projection is called non-truncated.

In cone-beam CT systems, the x-ray beam forms a conical geometry between the source and the detector. This is in contrast to conventional fan-beam geometry, as shown in Figure 2.6, in which the collimator restricts the x-ray beam to approximately 2D geometry. In the Fan-beam single detector arc geometry, data acquisition requires both rotation and z-direction translation of the gantry to eventually construct an image set composed of multiple axial sections. In cone-beam CT systems, an entire volumetric dataset can be acquired with a single rotation of the gantry. Incident photons on multiple-row detectors actually fall on a 2D area of detectors, as with flat-panel detection; indeed, with increasing numbers of rows in multiple-row CT detector arrays, the acquisition geometry actually approximates that of a cone-beam system.

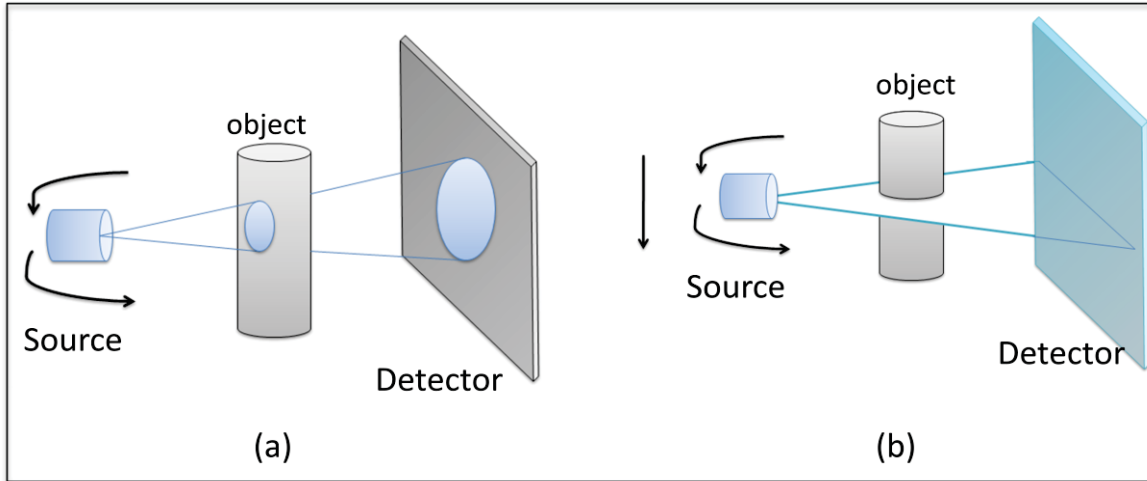


Figure 2.6 Depiction of CT acquisition geometries:
 (a) Cone-beam geometry, (b) Fan-beam geometry.

2.2.2 Projection matrix

Proper tomographic reconstruction depends on accurate calculation of the true location of the projection of each image voxel onto the detector plane. One approach to ensure this accuracy is to use a mechanically rigid system, such as in conventional CT. For systems which display some degree of mechanical deformation or instability during rotation, to achieve maximal image quality the true system geometry should be measured throughout the acquisition and incorporated into the reconstruction algorithm. With this assumption, the system geometry can be determined once and used to correct subsequent acquisitions.

Let a voxel of the 3D tomographic data is $P = (X, Y, Z, 1)$. The projection of the voxel P onto the pixel $p = (\lambda_x, \lambda_y, \lambda)^T$ of the projection plane is simulated by a pinhole perspective model, as shown in equation (2.4). According to (Wen P.L. et al., 2015), the pinhole perspective projection model is closest to the radiographic projection of the C-Arm acquisition systems. And hence, the projection is supposed to be perfect in which the distortions of the image mainly due to the influence of the terrestrial magnetic field on the trajectory of the photons X are supposed to be corrected (Lv et al., 2009).

$$p = F \cdot K_{\text{intrinsic}} \cdot K_{\text{extrinsic}} \cdot P \quad (2.4)$$

$$K_{\text{intrinsic}} = \begin{pmatrix} \alpha_i & 0 & c_i & 0 \\ 0 & \alpha_j & c_j & 0 \\ 0 & 0 & 1 & 0 \end{pmatrix} \quad K_{\text{extrinsic}} = \begin{pmatrix} R_s^T & -t_s \\ 0 & 1 \end{pmatrix} \quad F = \begin{pmatrix} f_1 & 0 & 0 \\ 0 & f_2 & 0 \\ 0 & 0 & f_3 \end{pmatrix}$$

The matrix $K_{\text{intrinsic}}$ includes intrinsic parameters of the projection. It characterizes the projective X-ray process. They are independent from the X-ray source point of view and encode for:

- The magnification induced by the projection process, that is associated with the relative position of the source with respect to the detector.
- The detector orientation which corresponds to the projection of the X-ray source.

The intrinsic matrix describes how a 3D voxel is projected onto the projection plane. The point (c_i, c_j) is the principal point, the center of the image in pixels in the frame (\vec{i}, \vec{j}) . It is the intersection of the optical axis with the plane of projection. Two parameters α_i and α_j are the focal lengths along the axes (\vec{i}, \vec{j}) . Let SID is the main focal length, and (ps_i, ps_j) is the size of the pixels in millimeters along the axes (\vec{i}, \vec{j}) of the image coordinate system, α_i and α_j are defined as:

$$\begin{aligned} \alpha_i &= -\frac{SID}{ps_i} \\ \alpha_j &= -\frac{SID}{ps_j} \end{aligned} \quad (2.5)$$

The matrix $K_{\text{extrinsic}}$ includes extrinsic parameters of the projection. Using the extrinsic parameters, it is straightforward to find the relation between the absolute coordinates of a real point and its relative coordinates in the X-ray source referential. This makes it possible to express the coordinates P of the voxels of the 3D tomographic data from the point of view of

the projection source. The matrix R_s and the vector t_s are respectively the rotation matrix and the translation vector of the transformation of the source:

- The rotation matrix encodes for the orientation of the X-ray source. The rotation matrix is composed of three independent rotations, parameterized by the Euler angles θ , γ and φ .

$$R_s = \begin{bmatrix} \cos \gamma \cos \varphi & \sin \theta \sin \gamma \cos \varphi - \cos \theta \sin \varphi & \cos \theta \sin \gamma \cos \varphi - \sin \theta \sin \varphi \\ \cos \gamma \sin \varphi & \sin \theta \cos \gamma \sin \varphi - \cos \theta \cos \varphi & \cos \theta \sin \gamma \sin \varphi - \sin \theta \cos \varphi \\ -\sin \gamma & \cos \gamma \sin \theta & \cos \varphi \cos \theta \end{bmatrix} \quad (2.6)$$

- The translation vector encodes for the position of the source within the 3D real world coordinate system. The origin of the system is set arbitrarily. For CT, it is fixed at the iso-center. The translation between the object and source coordinate system is :

$$t_s = \begin{bmatrix} t_x \\ t_y \\ t_z \end{bmatrix} \quad (2.7)$$

The matrix F makes it possible to invert the coordinates of the pixels to make them correspond to the 2D reference mark of the image (\vec{i}, \vec{j}) .

The projection matrix is derived from the intrinsic and extrinsic parameters of the projection, and is represented by the series of transformations.

$$A = K_{\text{intrinsic}} \cdot K_{\text{extrinsic}} \quad (2.8)$$

2.3 3D CT reconstruction

2.3.1 Fourier transform

The Fourier transform is a crucial component of most 3D CT image reconstruction algorithms. The Fourier transform provides a visualization of any waveform in the real world into a sum of sinusoids, providing another way to interpret waveforms. The function transforms a function of time into the frequency domain. The Fourier transform is useful because at times there are computations which are easier to calculate in the frequency domain rather than the time domain. In this research, the Fourier transform will transform functions in the time domain to the frequency domain for use in back projection and filtering within 3D CT image reconstruction algorithms.

Let $f(x, y)$ denote the object need to be captured by a CT system. The sources and detectors are oriented at an angle θ such that the latter records the contributions of $f(x, y)$ along the line $x\cos\theta + y\sin\theta = r$ for different values of r . Mathematically, the captured signal $f(r, \theta)$ can be expressed as the Radon transform of the object that is to be reconstructed. The Radon transform is defined as the equation (2.9).

$$f(r, \theta) = \int_{-\infty}^{\infty} \int_{-\infty}^{\infty} f(x, y) \delta(r - x \cos \theta + y \sin \theta) dx dy \quad (2.9)$$

where, $\delta(\cdot)$ is the delta function.

The CT image reconstruction can then be stated mathematically as recovering $f(x, y)$ from $f(r, \theta)$ for a collection of θ . The actual process of the reconstruction actually depends on a Fourier transform relationship, called the projection slice theorem. It states that the one-dimensional Fourier transform of the projection of a two-dimensional signal is equal to the slice of its two-dimensional at the same angle. This theorem provides the basis for practical reconstruction methods such as filtered back-projection.

2.3.2 Filtered Back-projection

The projection slice theorem and the inversion formula for the Fourier transform give an inversion formula for the Radon transform, as mentioned in section 2.3.1, often called the filtered back-projection (FBP). The filtered back-projection formula can be decomposed into two stages:

- The first stage is the application of a linear, shift-invariant filter to the Radon transform.
- The second stage is an angular back-projection (BP) of the filtered Radon transform.

2.3.2.1 Filtering

In electrical engineering and signal/image processing, filters are used to transform signals from one form to another, specifically to eliminate various frequencies in a signal. Filtering is usually needed to compensate for noise in data. A common approach for extracting the desired signals from the raw data is to convolve the filter with the Radon transform of the input data. In practice, functions representing the filters are usually defined in the frequency domain (Fourier). Thus, the filtering is performed as a multiplication in the frequency domain instead of convolution in the spatial domain.

The most used filter for reconstructing projections is Ramp filter. It is a high-pass filter, increasing frequencies above the cut off and decreasing low frequencies. It is used to create a clearer image without changing projection data before the back projection step. This filter assists in reducing blur and other visual artifacts found in the projection images. The Ramp filter, defined by the inverse Fourier transform targets image noise and imperfections and smooths them out through filtering techniques. The Ramp filter is demonstrated as Figure 2.7, with Ramp filter in frequency domain (left) and corresponding spatial domain filter (right).

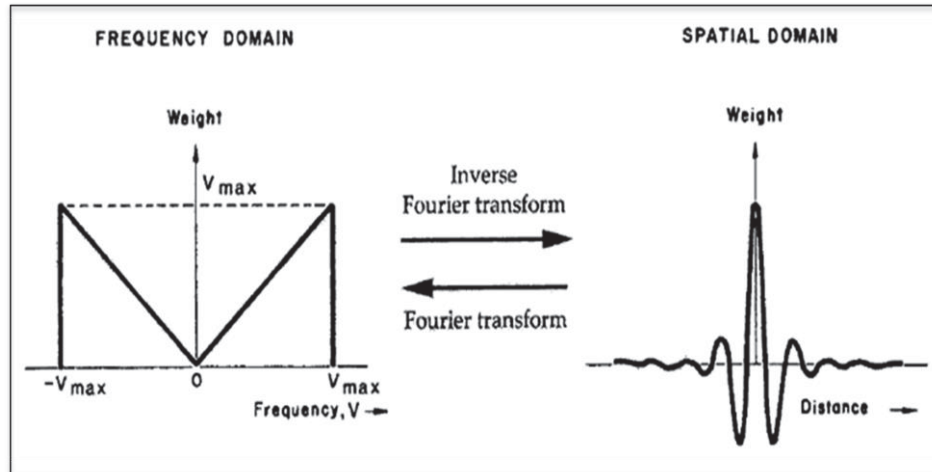


Figure 2.7 Ramp Filter

First, the Fourier Transform is calculated, then the Ramp Filter is evaluated, and then the inverse Fourier Transform is calculated. The core of the Ramp Filter equation is written as follows:

$$H_R(k_x, k_y) = |k| = \sqrt{(k_x^2 + k_y^2)} \quad (2.10)$$

As this equation is applied to the frequency domain (after application of the Fourier Transform) k_x and k_y represent the frequencies at a certain point. One example of Ramp filtering is shown in Figure 2.8.

Figure 2.8 (a) represents the original phantom image prior to unfiltered back-projection reconstruction in Figure 2.8 (b). Due to the overlapping of image slices that have undergone the Fourier Transform, the resulting image is very unclear. Because of this, a high-pass filter, such as the Ramp Filter, must be applied to attenuate the lower frequencies and keep the higher frequencies in the image. The lower frequencies cause blur, and therefore data must be passed through a high-pass filter to reduce the blurring.

Figure 2.8 (c) is the result of applying the Ramp Filter to the back projected image.

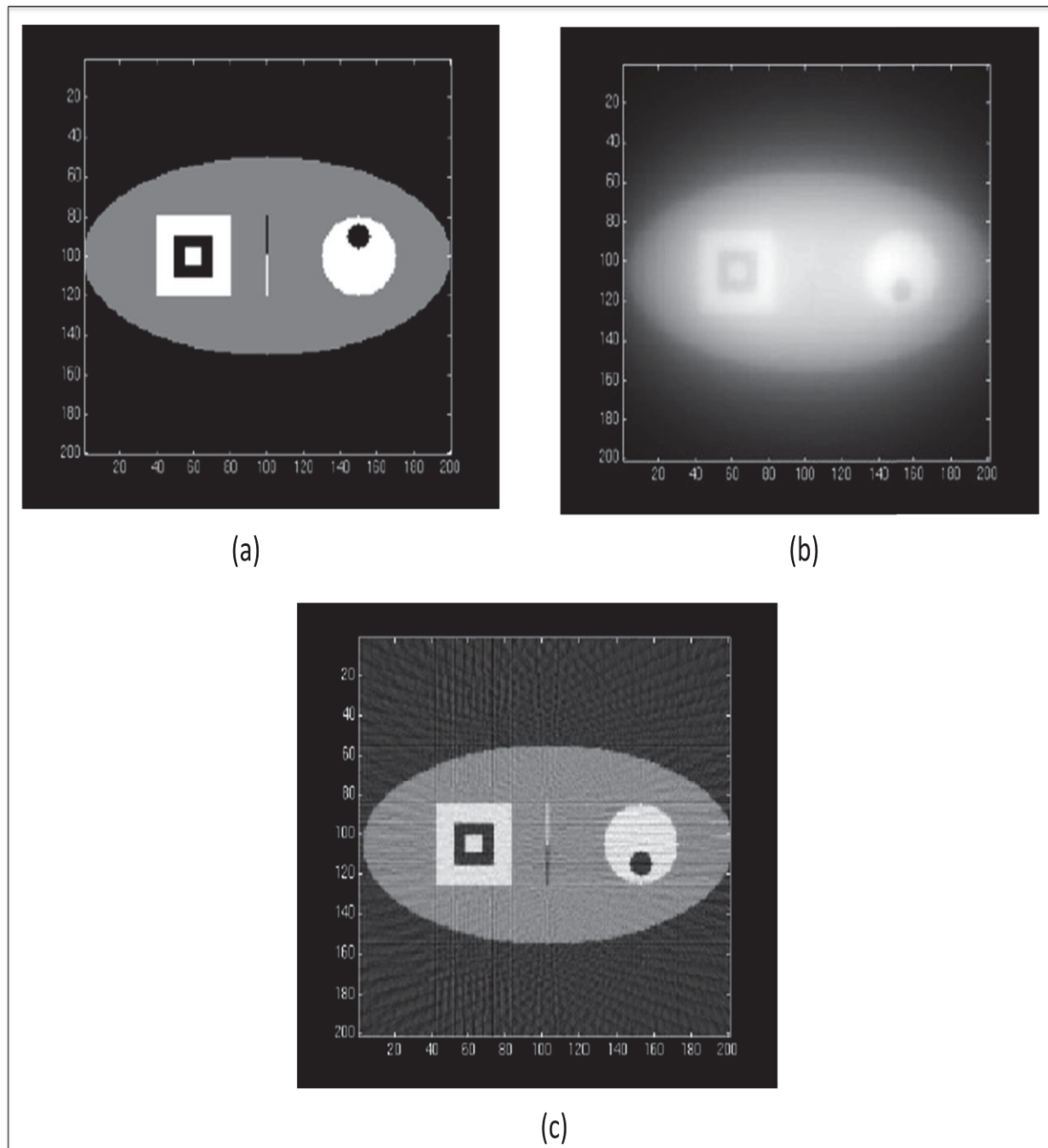


Figure 2.8 Ramp filtering example: (a) Original image, (b) Unfiltered back-projection, (c) Filtered back-projection.

The Ramp filter is usually multiplied by an apodizing window $W(r)$. The purpose of the apodizing window is to localize the support of the filter in the frequency domain (thereby suppressing noise). Common apodizing windows include:

➤ Hamming:

$$W(r) = (0.54 + 0.46 \cos(\frac{\pi r}{B})) X_{[-B, B]}(r) \quad (2.11)$$

➤ Hann:

$$W(r) = (0.5 + 0.5 \cos(\frac{\pi r}{B})) X_{[-B, B]}(r) \quad (2.12)$$

where, the characteristic function, $X[-B, B]$, is:

$$W(r) = \begin{cases} 1 & \text{if } r \in [-B, B] \\ 0 & \text{otherwise} \end{cases} \quad (2.13)$$

2.3.2.2 Back-projection

One commonly used way to display a full set of projection data is in the form of a 2-D matrix. A representation of this matrix, generically is known as a sinogram, as shown in Figure 2.9.

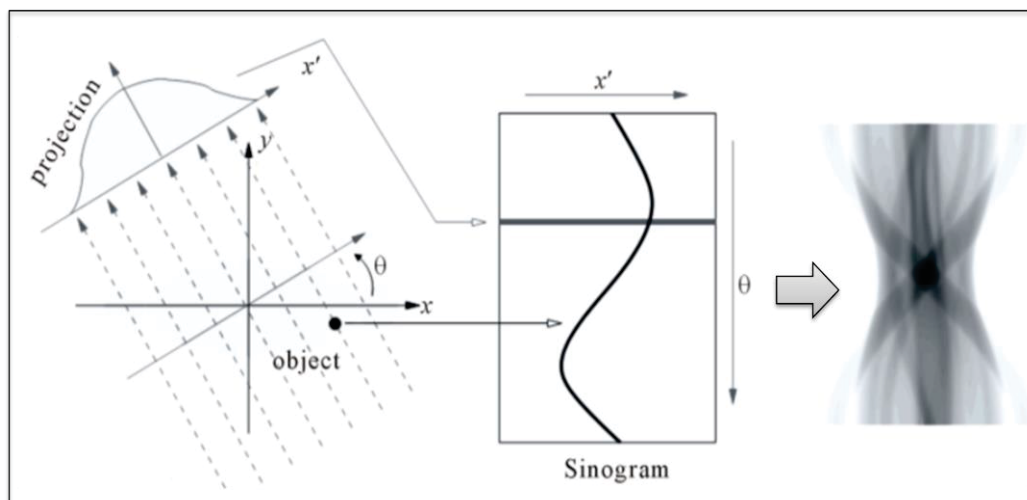


Figure 2.9 Sinogram.

Each row across the matrix represents an intensity display across a single projection and corresponding to an individual projection profile. The successive rows from top to bottom represent successive projection angles. The name sinogram arises from the fact that the path of a point object located at a specific (x, y) location in the object traces out a sinusoidal path down the matrix. The sinogram provides a convenient way to represent the full set of data acquired during a scan and can be useful for determining the causes of artifacts in CT images.

The back-projection operator reconstructs the object $f(x, y)$ from the sinogram $g(r, \theta)$ as follows. Along a particular scanning line $x\cos\theta + y\sin\theta = r$, the value of the projection $g(r, \theta)$ is assigned to all points (x, y) along that line. This is integrated or repeated for all ranging from 0 to π because projections acquired between π and 2π do not provide new information, as they are symmetric. This is given by:

$$\begin{aligned} f_{BP}(x, y) &= B\{g(r, \theta)\} \\ &= \int_0^{\pi} g(x \cos \theta + y \sin \theta, \theta) d\theta \end{aligned} \quad (2.14)$$

A specific situation of the filtered back-projection is illustrated in Figure 2.10. An object shown as a two-dimensional image consists of a group of points. Projections of this object are taken from different angles and the sum of all intensity along each projection path is presented, as shown in Figure 2.10 (a). In order to reconstruct the image, from each projection we re-distribute the activity in equal amount back to its original path, as shown in Figure 2.10 (b). This is called the summation algorithms as we are applying back-projection to projection data. The last step is the accumulation of ray-sums from all angles over 360° of all the rays passing by this point.

As shown in Figure 2.10 (b), the approached image is unsatisfactory as it is blurred and has a cone like shape. Therefore, a simple back projection is not sufficient to reach a good image. In order to obtain and sharpen the image, a filter must be applied to the projections as illustrated in Figure 2.10 (c).

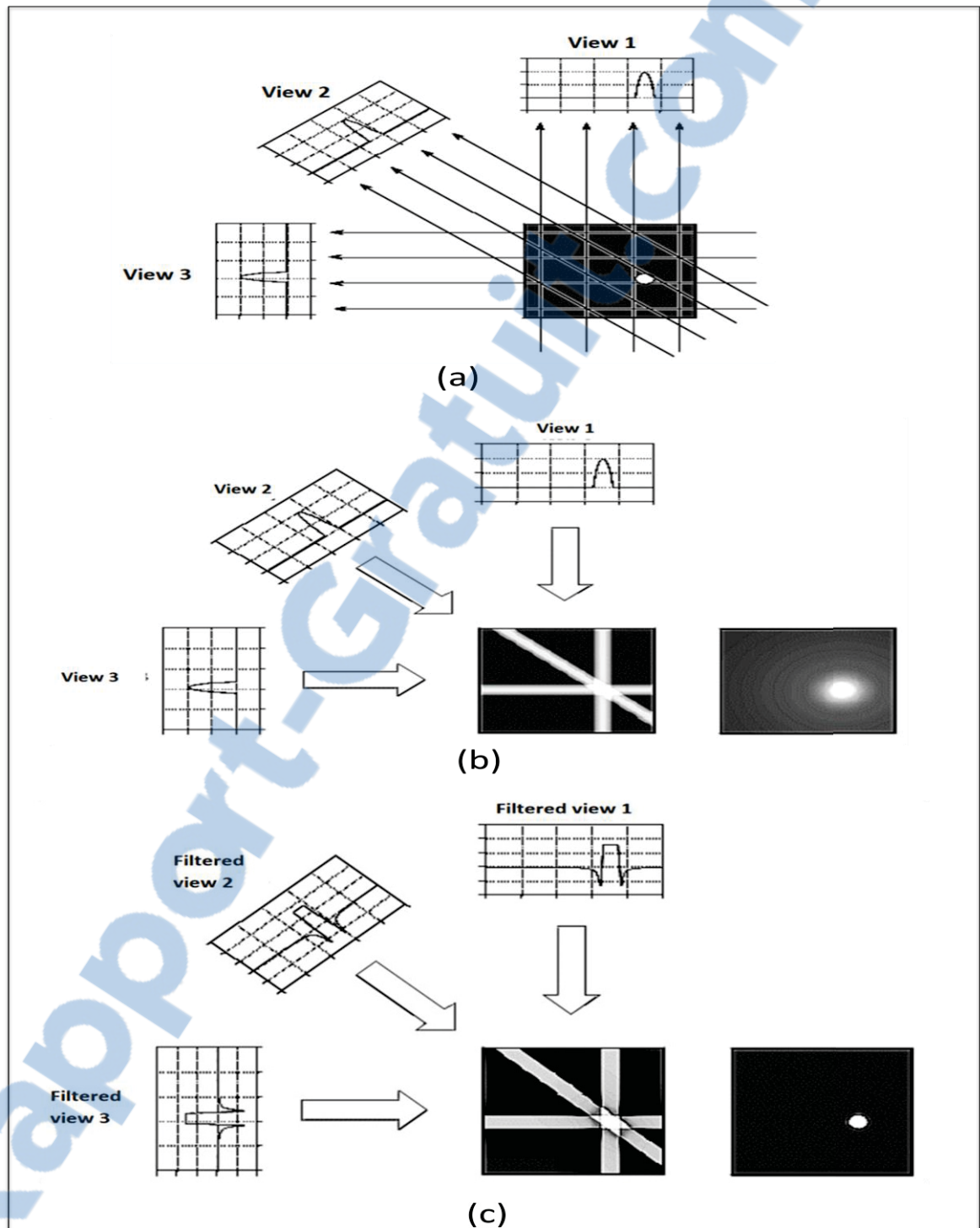


Figure 2.10 The Filtered back-projection process: (a) Projection, (b) Back-projection with blur, (c) Back-projection with the filter.

2.3.3 Cone beam reconstruction process

The process of CT image reconstruction begins with acquiring the data from the cone beam CT scanner, and then reconstructing the two dimensional images. This process not only creates the three dimensional representation of an object, but also essentially reduces the artifacts in the images.

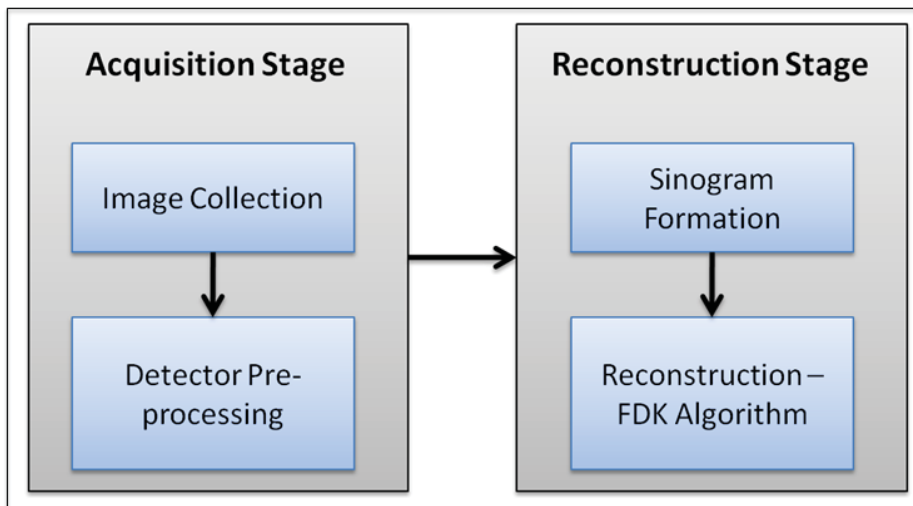


Figure 2.11 Cone beam CT reconstruction process.

The reconstruction process consists of two stages, as shown in Figure 2.11:

- The first stage in cone beam CT image reconstruction is the acquisition stage, beginning with image data collection. Because of the spatially varying physical properties of the photodiodes and the switching elements in the flat panel, and also because of variations in the x-ray sensitivity of the scintillator layer, raw images from cone beam CT detectors show spatial variations of dark image offset and pixel gain. To compensate for these inhomogeneities, raw images require systematic offset and gain calibration and a correction of defect pixels. The sequence of the required calibration steps is referred to as “detector pre-processing” and the calibration requires the acquisition of additional image sequences (Nassir N. et al., 2010). As the result of the calibration step, the intrinsic parameters and the extrinsic parameters of the system will be generated.

- The second stage in the cone beam CT process is the reconstruction stage. This stage involves processing image relations and recombining slices to create a three dimensional volume. This stage involves constructing a sinogram, a composite image relating each row of each projection image, as shown in figure 2.8. A reconstruction filter algorithm is applied to the sinogram and converts it into a complete 2D CT slice. The filtered back projection algorithm used for cone beam acquired volumetric data is the FDK algorithm. Once all the slices have been reconstructed, they can be recombined into a single volume for visualization.

2.3.4 FDK algorithm

The FDK algorithm reconstructs a 3D volume from multiple 2D projections, a scanner along with a 2D detector takes a full rotation around the patient or object of interest to capture the data. In other words, the FDK requires a rather dense number of projections taken around 360°. When only a limited number of projections is available, the FDK as a filtered back-projection based method is affected by artifacts.

The FDK algorithm implements filtered back projection, heavily relying on the conversion from a cone-beam reconstruction problem to a modified fan-beam reconstruction problem.

The general FDK algorithm is performed based on the following steps:

- First, the raw data is individually weighted.
- Second, apply the ramp filtered to produce filtered projections.
- Third, back-projection step is performed.

Let $F(x,y,z)$ represents the value of voxel (x,y,z) in volume F . The projections are collected at a distance from X-ray source to detector, SID, with angle θ_i where $1 \leq i \leq N$ (N is the number of projections). The distance between the volume origin and the source is denoted by SOD. The volume is in xyz space and uv represents the projections that are to be back projected to

the volume, as shown in Figure 2.12. The volume F is reconstructed by using the following equation (2.15).

$$F(x, y, z) = \sum_{i=1}^N W(x, y, i) \cdot p_F(u(x, y, i), v(x, y, z, i)) \quad (2.15)$$

where, W is the FDK distance weight and $p_F(u, v)$ is the filtered projection data of the image u at pixel position v . The pixel position for back-projection to the voxel (x, y, z) is determined by the perspective projection A . The perspective projection A can be calculated using pre-calibrated projection matrices.

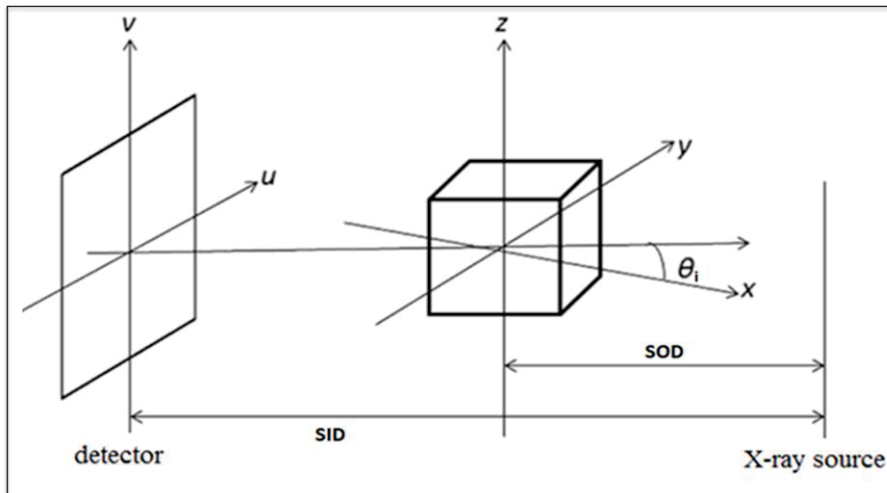


Figure 2.12 The coordinate system.

2.3.5 ECG-gated in FDK algorithm

Gating techniques are used to improve temporal resolution and minimize imaging artifacts caused by cardiac motion. Two approaches to cardiac gating are typically used: prospective ECG triggering and retrospective ECG gating.

The simplest technology for acquiring gated cardiac images is referred to as prospective gating or sometimes prospective ECG triggering. In this mode, the scanner monitors the patient's ECG. It is set to scan at a particular point in the cardiac cycle, which is typically in

diastole since the heart is moving the least then. The scanner interprets the ECG and determines a delay after the QRS complex to begin scanning. At that point, the ECG triggers the scanner to start scanning. The scanner must complete a 180 degree rotation in order to obtain a full image. It then waits for the next diastolic phase to scan the next part of the heart. For this reason, some people refer to this technique as "step and shoot" since the scanner moves the table in between successive diastolic phases.

Each scan has a certain z-axis coverage, which is determined by the width of the CT detector and pitch. To complete the cardiac CT, we need to cover the entire heart, which is typically around 12-15 cm. Thus, with wider detectors (more rows), the heart is captured in fewer beats. The problem with needing multiple beats is that the patient may move in between the beats; if the scan is really slow, the patient may even breathe which will change the position of the heart in the chest and make the scan uninterpretable.

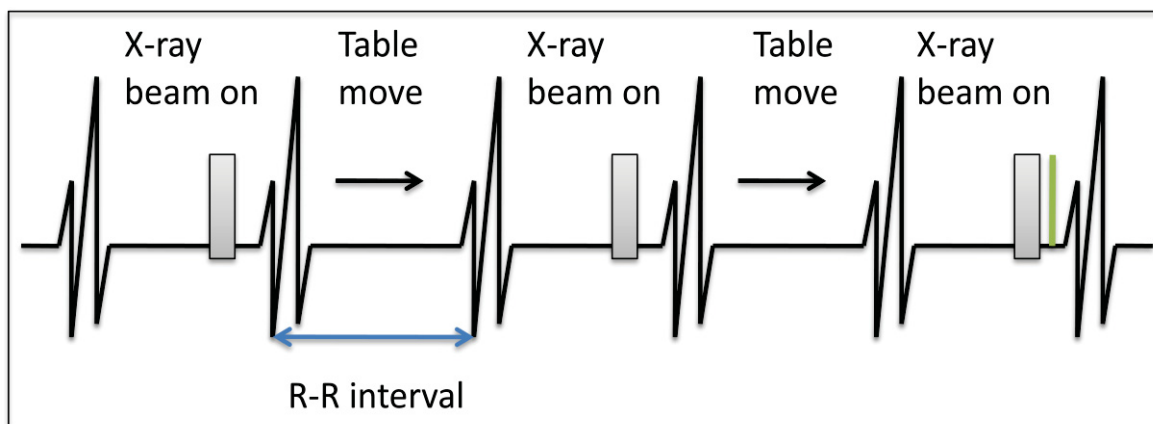


Figure 2.13 Prospective ECG triggering.

Figure 2.13 shows the example of prospective ECG-gated cardiac CT technologies. In this Figure, shaded gray denotes the times when the scanner tube is turned on and green line denotes the current time. In the R-R interval (the interval between two beats) between the two x-ray beams ON, the table can be moved.

As an alternative to prospective gating, the retrospective gating technique scans the patient continuously, although only certain portions of the scan are used to reconstruct the image. Because the scan spans all phases of the cardiac cycle, we can reconstruct images in systole,

diastole, or anywhere in between. This can be useful to obtain functional information and can also be helpful in patients where there is still some motion during portions of diastole, since we can pick slightly earlier or later phases to use for the reconstruction, as shown in Figure 2.14.

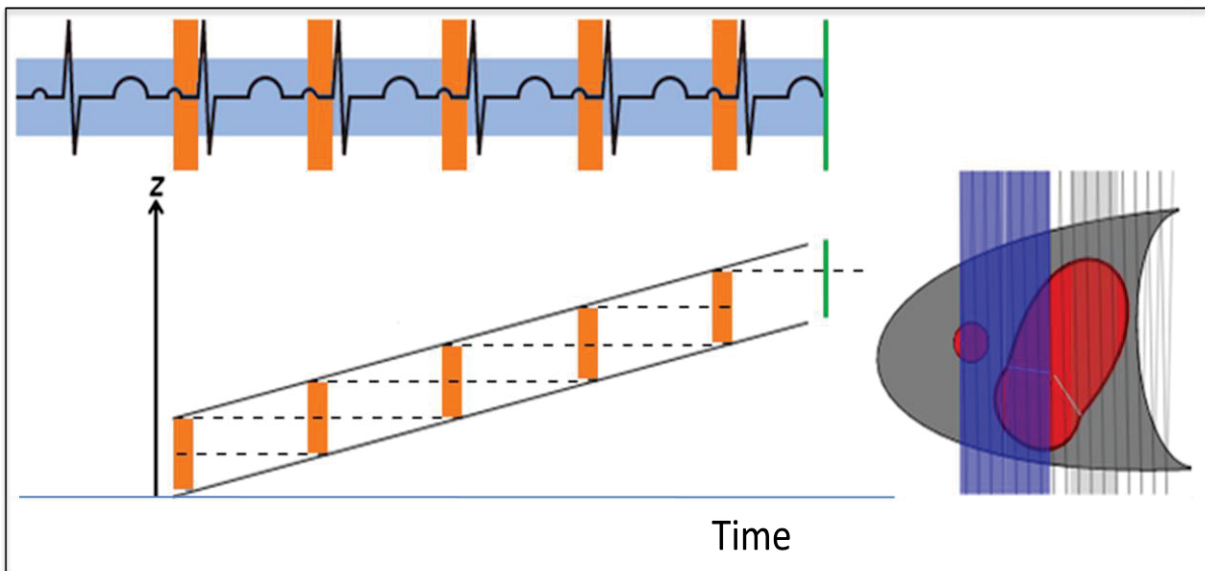


Figure 2.14 Retrospective ECG Gating.

In Figure 2.14, ECG tracing with green line denoting the current time of the top left. The tall orange boxes denote the portions of diastole used for reconstruction. The shorter shaded blue line is continuous - showing that the tube is ON during the entirety of the scan. In the bottom left, plot of the scanner position along the z-axis of the patient over time and orange boxes denotes the portions used for reconstruction of diastole. Dashed lines show any gaps or overlap in z-axis coverage (between successive diastoles). The heart is illustrated with current tube position denoted by the blue line and gantry helix displayed as gray lines as an entire detector width is completed, that region is shaded in blue.

In ECG-gated FDK reconstruction, an initial ECG-gated reconstruction is performed by inserting a weighting function ϕ into a standard FDK algorithm. The function ϕ is a weighting function that is used to obtain an ECG phase correlated reconstruction for the heart phase $h \in [0, 1]$. It is a cosine-window given by the equation below:

$$\phi(i, h) = \begin{cases} \cos^\alpha\left(\frac{d(h(i), h)}{\mu} \pi\right) & \text{if } d(h(i), h) \leq \frac{\mu}{2} \\ 0 & \text{otherwise} \end{cases} \quad (2.16)$$

Where, $h(i)$ is the heart phase of the i^{th} projection image according to the ECG,

The distance function $d(h_1, h_2)$ returns the distance between two heart phases,

$\alpha \in [0, \infty)$ controls the shape of the support region,

$\mu \in [0, 1]$ controls the width.

By using the ECG-gated FDK reconstruction, the volume F is reconstructed by using the following equation (2.17).

$$F(x, y, z) = \sum_{i=1}^N \phi(i, h) \cdot W(x, y, i) \cdot p_F(u(x, y, i), v(x, y, z, i)) \quad (2.17)$$

CHAPTER 3

EXPERIMENTS AND RESULTS

3.1 Experiment setup

The experiment is implemented by using data from the XCAT phantom (Segars *et al.*, 2010). This phantom contains anatomy information derived from real CT/MRI datasets, which allows the simulation of realistic datasets for cardiac C-arm CT. Projections are simulated using cone-beam imaging geometry with source to detector distance (SID) and source to object (SID) varies for each patient. The projection has a dimension of 512×512 pixels with an isotropic resolution of 0.5 mm/pixel. The reconstruction volume has a dimension of $256 \times 256 \times 256$ voxels with isotropic resolution of 0.5 mm/voxel. There are 75 projection images covering an equiangular range of 360° with the acquisition time is $T = 0.053$ s, as describe in Figure 3.1.

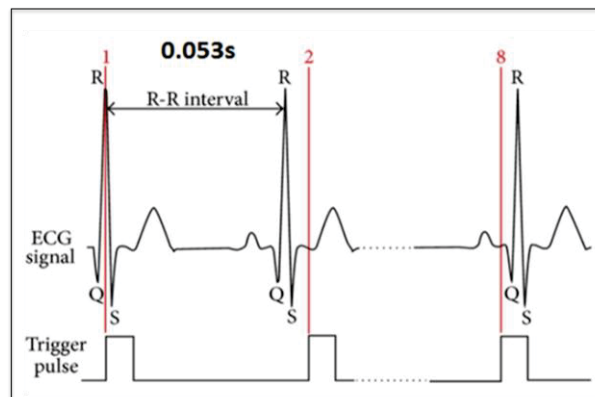


Figure 3.1 The acquisition time.

The experiment was conducted with four patients with different ages including men and women. These patients have the physical characteristics as shown in Table 3.1.

Table 3.1 The physical characteristics of patients

Patient	Arteries	SOD(mm)	SID(mm)
#1	LCA& RCA	650	900
#2	LCA&RCA	670	900
#3	LCA	650	920
#4	RCA	700	940

For each patient, there are three datasets which are generated from XCAT phantom that we can use to reconstruct the 3D model of coronary artery follow FDK algorithm. First, the projection dataset with periodic cardiac vasculature motion is obtained by ray-driven forward projection. Second, the projection dataset with an aperiodic combination of cardiac and breathing motion is created analogously to the first dataset. In addition to the same cardiac motion pattern, the XCAT software is configured to simulate a breathing motion with a cycle time of 4s. Finally, another projection dataset is obtained without motion. These datasets are shown in Figure 3.2.

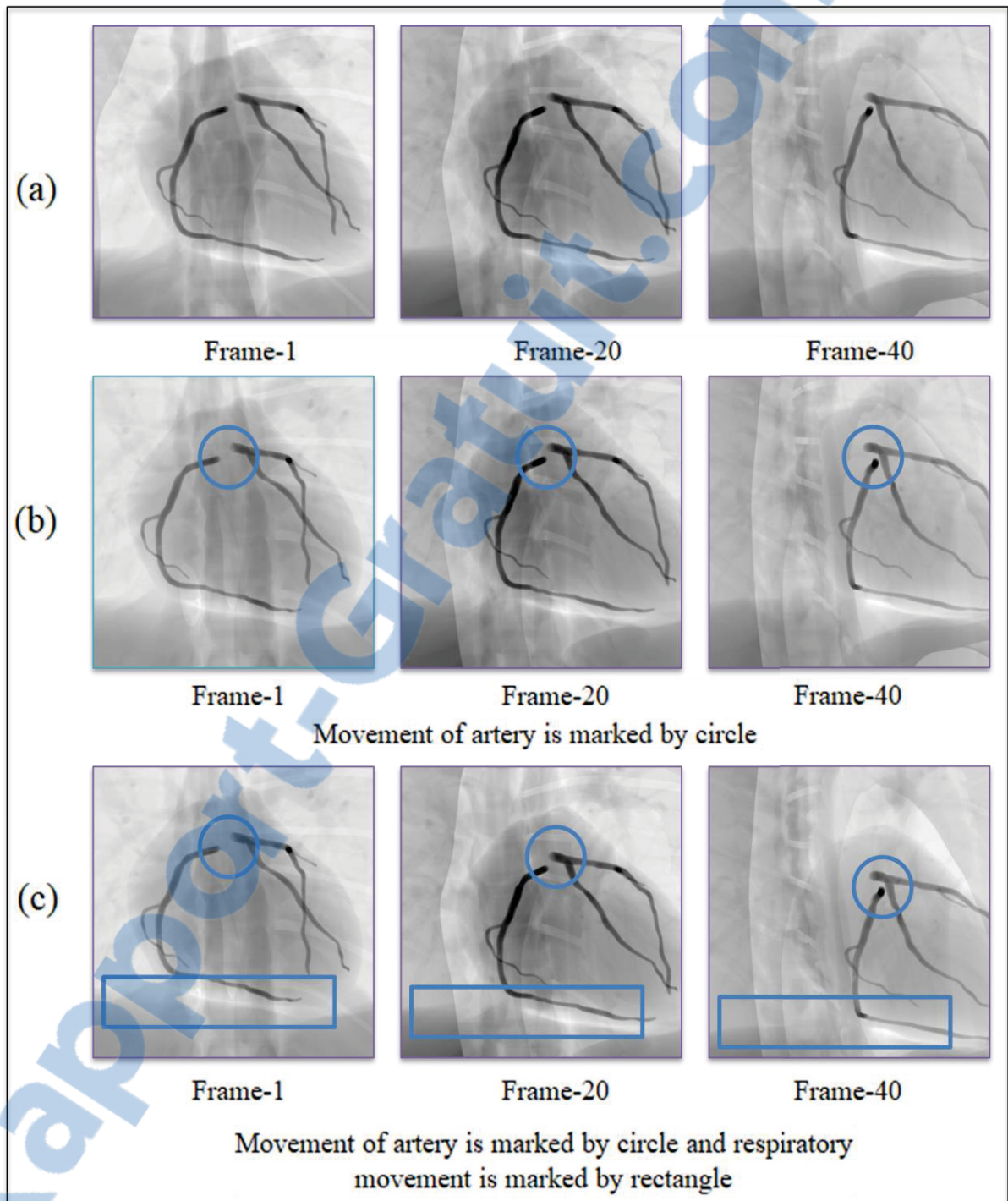


Figure 3.2 Three datasets generated from XCAT phantom: (a) Dataset without motion, (b) Dataset with cardiac motion, (c) Dataset with both motion.

In two datasets with motion, the motion phase signal for the cardiac motion and the motion phase signal for the respiratory motion are depicted in Figure 3.3. This motion phase is built based on the real data to evaluate the quality of each projection image.

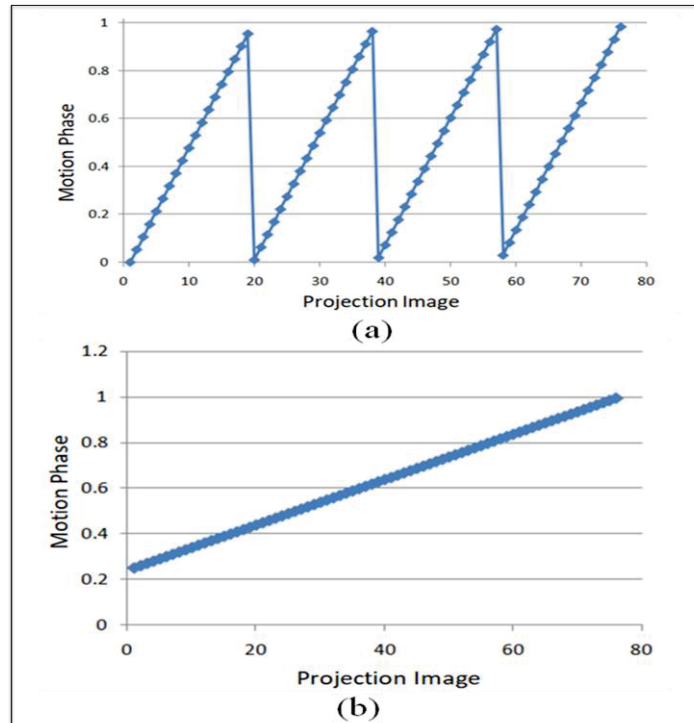


Figure 3.3 The motion phase signal: (a) For cardiac motion, (b) For respiratory motion.

3.2 Evaluation and result

To evaluate the overlapping effect between coronary artery vessels, projection images data of patient-1 will be taken with different gantry orientations. As mentioned in section 2.1, the gantry orientation can be change by adjusting two values θ and φ . In this experiment, we will focus about the overlapping effect between two branches of the left coronary artery: left anterior descending artery and circumflex artery. The overlapping areas between those two branches show in Figure 3.4 with different pair of angles (θ , φ).

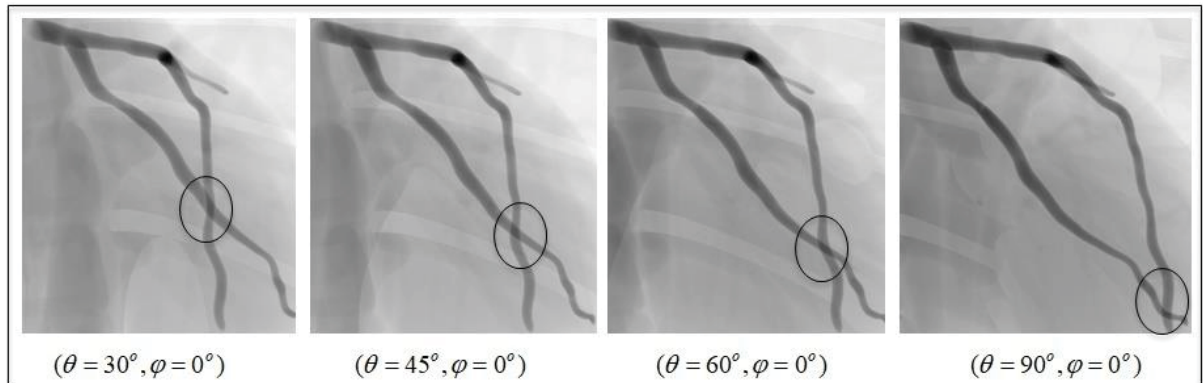


Figure 3.4 The overlap area between the left anterior descending artery and the circumflex in different gantry orientations.

To measure the area overlap between two vessels, the diameter of each vessel need to be estimated by extracting the centerline. As illustrated in Figure 3.5, the left coronary artery need to be highlighted the edge of vessels by using Frangi filter. Then the centerline is extracted, and the diameter of the vessel can be estimated by calculating the mean distance.

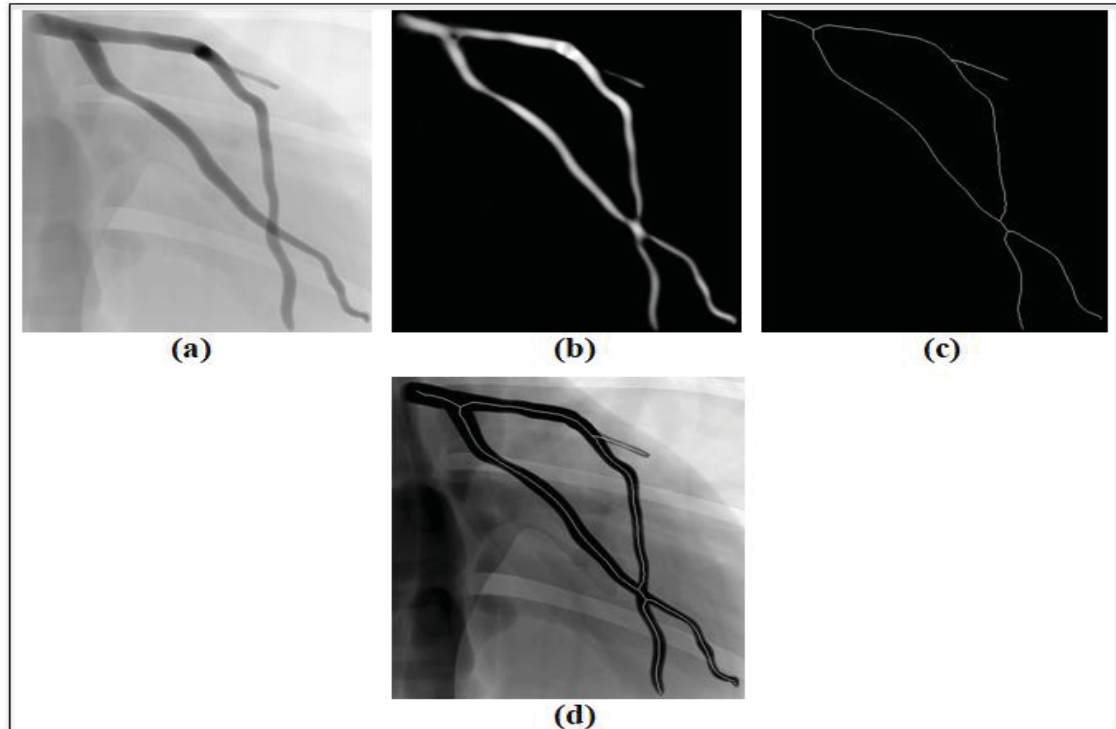


Figure 3.5 Extracting centerlines for the projection image with $(\theta = 45^\circ, \varphi = 0^\circ)$:
 (a) Original image, (b) Highlight the vessels, (c)-(d) Extract the centerlines.

Based on the equation (2.2), the rate of overlapping between two branches, left anterior descending artery and circumflex artery, will be calculated and shown in Table 3.2 for each gantry orientation.

Table 3.2 Rate of overlapping between two branches
in different gantry orientations.

Gantry orientation (θ, φ)	Rate of overlapping (%)
(30°,0°)	18.5
(45°,0°)	16.4
(60°,0°)	17.8
(90°,0°)	14.9

It is difficult to evaluate directly the foreshortening effect without the real C-arm system. In this experiment, the 3D model of coronary artery will be reconstructed with different gantry orientations. Then the quality of each model will be calculated by using Dice coefficient to evaluate the foreshortening effect.

The quality assessment is performed using the Dice similarity coefficient (DSC), a measure of spatial overlap. Generally speaking, the DSC represents the size of the union of two sets divided by the average size of the two sets. This normalized evaluation measure is a proven method in the segmentation literature for assessing the quality of a binary segmentation given a ground truth.

Commonly, the DSC measures the spatial overlap between two target regions, A and B, and is defined as:

$$DSC(A, B) = 2(A \cap B) / (A + B) \quad (3.1)$$

where, \cap is the intersection.

The Dice similarity coefficient has the value within range of $[0, 1]$, as illustrated in Figure 3.6.

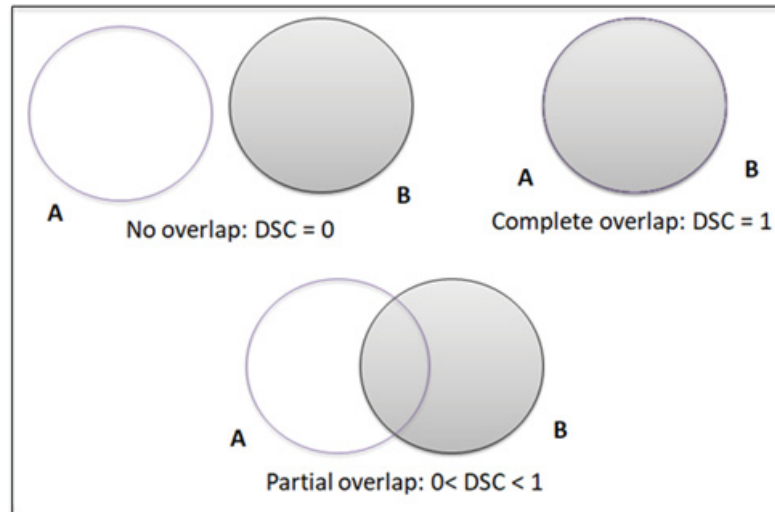


Figure 3.6 The Dice similarity coefficient.

The quality of the reconstruction f can be determined by each of the total ground true phantom volumes f_i . At the projection image i , the quality of the reconstruction f can be measured by the following equation:

$$q_i = DSC(f_i, B(f, s)) \quad (3.2)$$

With $B(f_i, s)$ is a ground true which returns the binary volume of the volume f with all elements being one if they are larger than or equal to the threshold number s at the projection image i . The binary volume has a good quality with high contrast. Thus, it is compared to the volume f by using the Dice similarity coefficient. The Dice similarity coefficient value ranges from “0” to “1”, with “1” corresponding to a perfect match. The Dice similarity coefficient between two volumes is calculated by using equation (3.1).

The number s of the 8-bits reconstruction f varies from 0 to 255. Thus, the quality measure of the reconstruction f at the projection image i is given by:

$$q_i = \max_{0 \leq s \leq 255} DSC(f_i, B(f, s)) \quad (3.3)$$

For each projection image i , the threshold value s corresponds to the maximum DSC at which the quality measure q_i of projection image i is best. As shown in Figure 3.7 with the dataset of patient-1, the quality measure of the reconstruction f at the projection image 25 approximates 0.263.

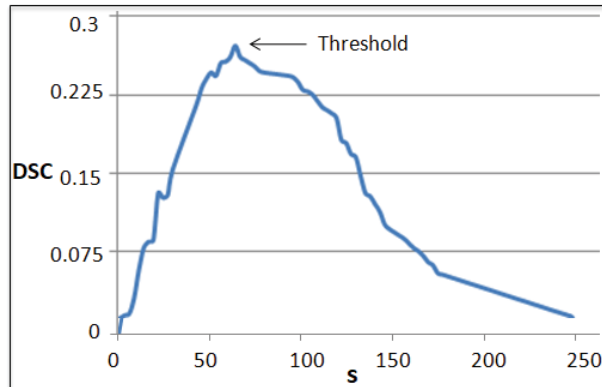


Figure 3.7 The quality measure of f at the projection image 25 of patient 1.

The quality of reconstruction f at each projection image of patient-1 with motion is illustrated in Figure 3.8.

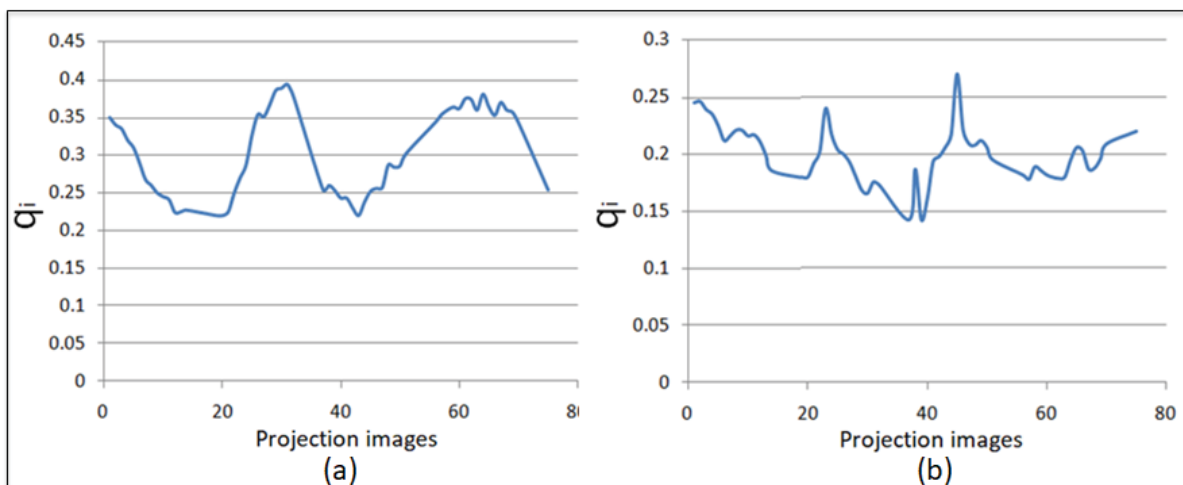


Figure 3.8 The quality measure of f at each projection image of patient-1:
(a) With cardiac motion, (b) With cardiac and respiratory motion.

It can be seen that the motion phase (as shown in Figure 3.3) affects to the quality of the reconstruction. For each projection image, it has a different quality value. When the cardiac motion added, the quality of the reconstruction is still smoothly. However, the quality of the reconstruction is more complicate to evaluate when adding the respiratory motion.

The quality of a single 3D reconstruction can be measured by searching the projection image whose the quality of the reconstruction at that projection image is best. Thus, the quality of the reconstruction f is given by:

$$Q = \max_{1 \leq i \leq N} q_i \quad (3.4)$$

with N is the number of projection images.

Before applying for all patients, the 3D model of coronary artery of patient-1 will be reconstructed with different gantry orientations. Based on the Dice coefficient the quality will be evaluated for each gantry orientation, and hence the best gantry orientation will select at which Q is maximum. Table 3.3 shows the value of Q for different pair of angles (θ, φ) .

Table 3.3 The quality of the 3D reconstruction for patient-1 in different gantry orientations.

Gantry orientation (θ, φ)	Quality (Q)
$(30^\circ, 0^\circ)$	0.165
$(45^\circ, 0^\circ)$	0.206
$(60^\circ, 0^\circ)$	0.147
$(90^\circ, 0^\circ)$	0.337

Based on results from Table 3.2 and Table 3.3, it can be seen that the pair of angles $(\theta = 90^\circ, \varphi = 0^\circ)$ given a good working view of the 3D reconstruction. With this gantry orientation, the overlapping effect and the foreshortening effect are noticeably improved. The pair of angles $(\theta = 90^\circ, \varphi = 0^\circ)$ will be use for other patients in this experiment to reconstruct the 3D model of coronary artery.

The model of 3D reconstruction using the ECG-gated FDK algorithm is shown in Figure 3.9 for four patients. Besides, the quality of each 3D reconstruction with cardiac motion is calculated by equation (3.4) to compare with ground true and shown in Table 3.4.

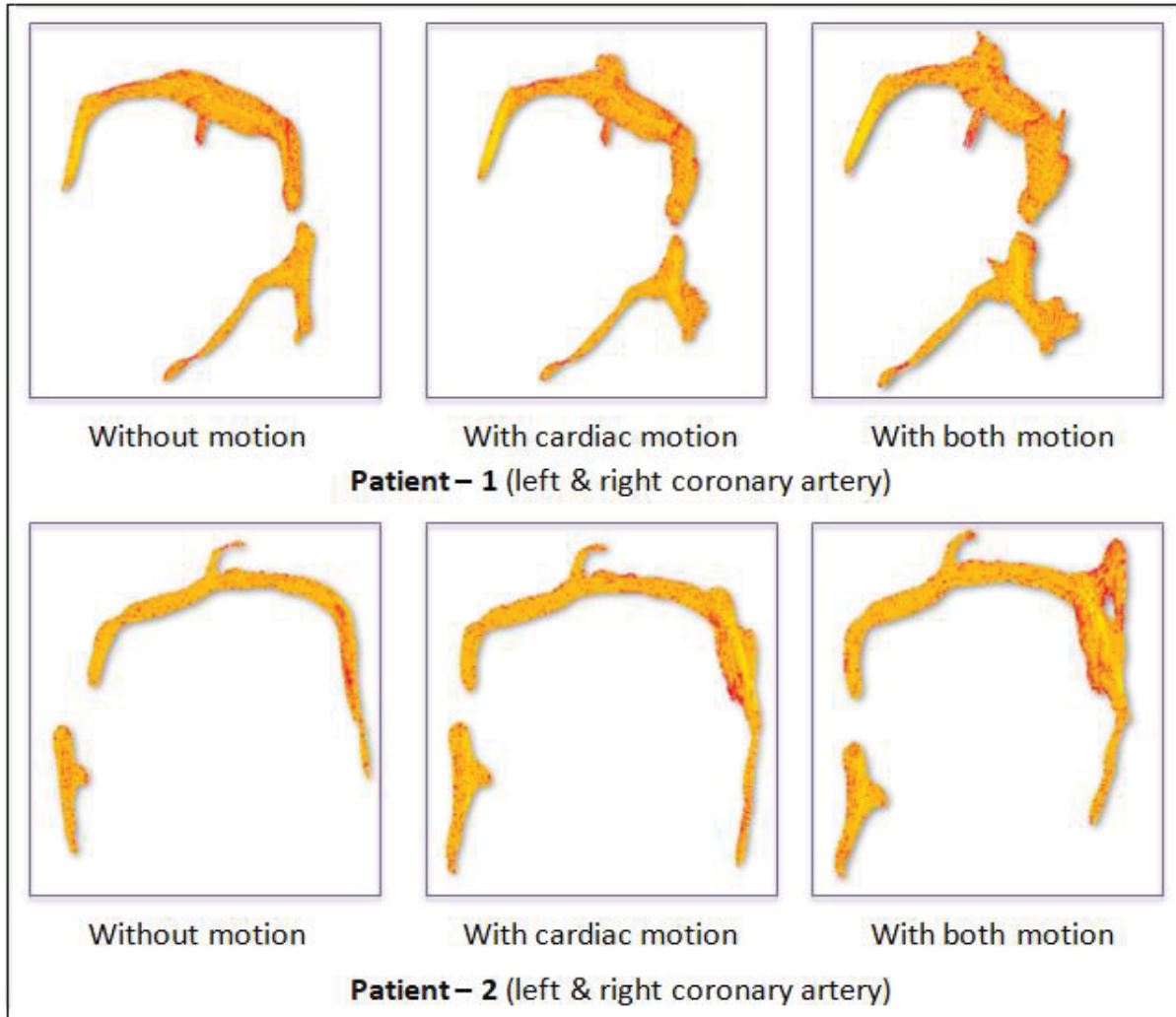


Figure 3.9 3D reconstruction of coronary artery using FDK.

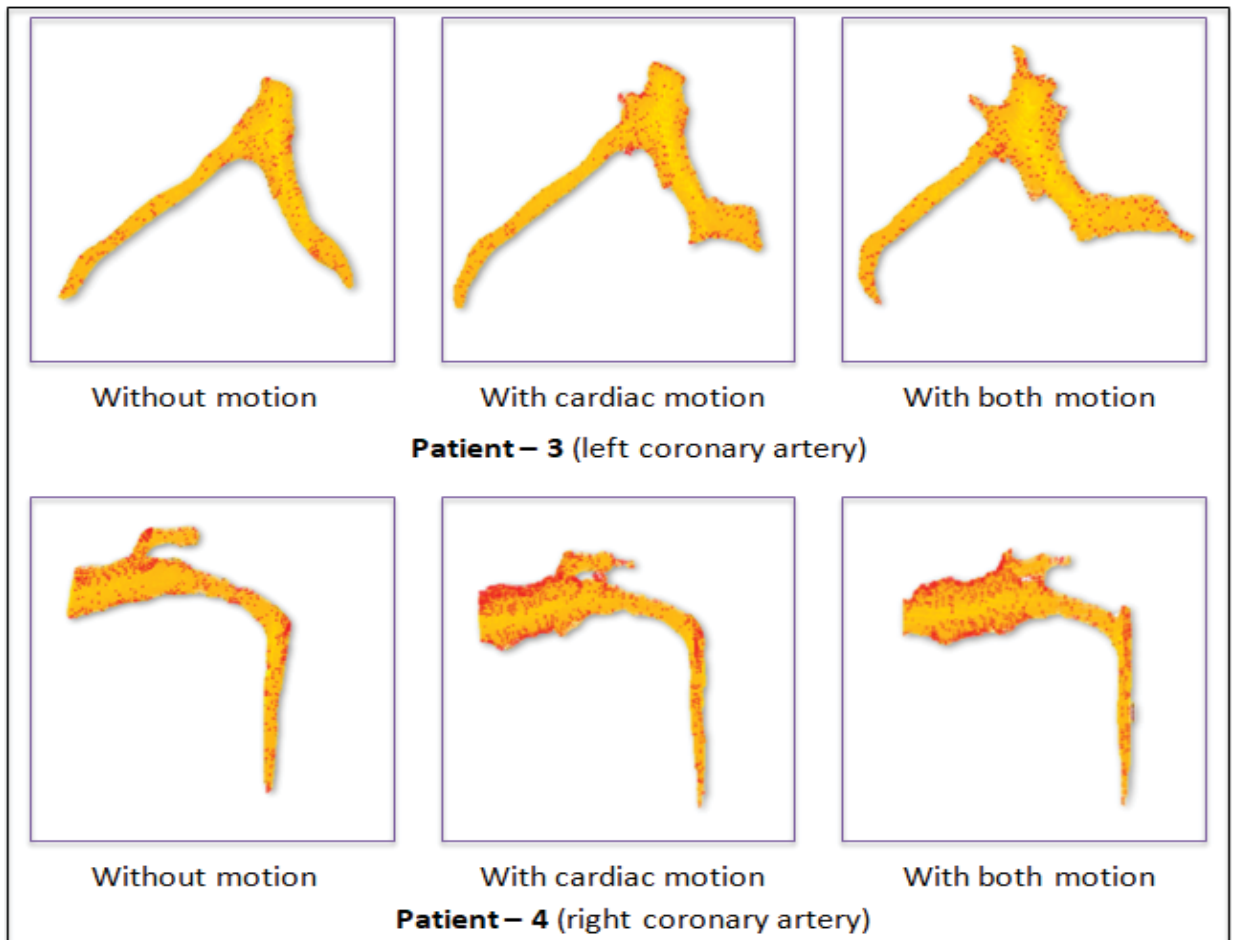


Figure 3.9 3D reconstruction of coronary artery using FDK (cont.).

Table 3.4 The quality of the 3D reconstruction for each patient with cardiac motion (when comparing with ground true)

Patient	Quality (Q)
#1	0.356
#2	0.329
#3	0.335
#4	0.343

It can be seen that the quality of the reconstruction is quite good when using ECG-gated FDK technique. The cardiac motion was compensated, hence the value of Q is stable. It is not much affected by the cardiac motion.

As shown in Figure 3.9, the 3D reconstruction of coronary artery is present for each patient in three cases: without motion, with cardiac motion and with both motion (cardiac motion and respiratory motion). When motion model is applied to the reconstruction, the quality of 3D reconstruction is decrease with more artifacts appearing on the 3D model.

In this 3D reconstruction algorithm, the gating parameter is an important parameter. It is a 2D vector containing the gating configuration. It includes two elements. The first element is the target reconstruction heart phase and the second element is the gating function window width. The effect of this parameter on quality of 3D reconstruction is considered through Table 3.5 and Table 3.6 for patient-1.

In Table 3.5, the width of the gating function window is kept at a value. Then the 3D reconstruction of coronary artery is implemented by using FDK algorithm with the heart phase varies from $\pi/2$ to $\pi/6$. It can be seen that the quality of 3D reconstruction is maximum at the value $\pi/2$ and then decrease as the heart phase increase.

In Table 3.6, the heart phase is kept at $\pi/6$ at which will be generated the good 3D model. Then the 3D reconstruction of coronary artery is also implemented by using FDK algorithm with the gating function window width varies from 30% to 90%. It can be seen that the good quality of 3D reconstruction can be obtained with the gating function width around 50%. When the gating function window width decreases or increases from this value, the quality of 3D reconstruction is also decreases.

Table 3.4 The relation between quality of 3D reconstruction and the heart phase of patient-1

Heart Phase	Quality (Q)
$\pi/2$	0.31
$\pi/3$	0.277
$\pi/4$	0.268
$\pi/6$	0.253

Table 3.5 The relation between quality of 3D reconstruction
And the gating function window of patient-1

The gating function window width	Quality (Q)
30%	0.298
50%	0.337
70%	0.285
90%	0.279

CONCLUSION

During last decade, 3D model generation from a traditional X-ray angiography of coronary artery has important clinical value in cardio vascular disease. Many studies have been invested to improve the reconstruction methods for coronary artery. Most of current 3D reconstruction methods are based on multiple projections instead of using two projections. With the incorporation of multiple projections, the reconstruction method is more efficiently to simulate a complex coronary artery tree. Because it may be more easily to find the optimal views with a sufficient contrast injection and minimal vessel overlap/ foreshortening for the complete coronary artery tree.

Recently, 3D reconstructions of coronary artery are being integrated into percutaneous coronary interventions (PCI). One of the most important applications is optimal view selection using reconstructions. Follow this approach way, optimal views are obtained without additional radiation which may help to position the stent, and hence, the contrast material used is reduced. In the near future, dynamic reconstructions need to be developed which can be provided a truly 3D display of the coronary arteries for helping clinicians in surgery.

The method that was proposed in this study is about 3D reconstruction of arteries coronaries for a rotational angiographic sequence. It was intended to satisfy the goal of providing a method with robust results that can be executed in an interventional context. To achieve the goal, the dual-axis coronary artery angiography is used to acquire data from the patient. This technique is necessary about the reduction in the radiation dose as well as the enhancement quality of 3D reconstruction. A new method is proposed to working with the dual-axis rotational angiography. By using this method the physician is be able to select the optimal working view, hence the quality of coronary artery images can be improved and avoiding foreshortening and overlapping effects between coronary artery vessels. Then the ECG-gated FDK reconstruction algorithm was proposed to reconstruct 3D model of coronary artery. This is a dynamic reconstruction algorithm. By using this method cardiac motion can be

compensated during reconstruction time, hence the quality of 3D coronary artery model could be improved and reduced the reconstruction time. Overall, the proposed method is automatic and runs in an interventional context to provide robust results and fast execution. The combination of dual-axis angiography technique and ECG-gated FDK algorithm will provide a powerful support tool for clinician in surgery for cardiovascular disease.

The main difficulties that arise for the 3D reconstruction of coronary arteries from angiograms are indeed the respiratory and cardiac motions that are visible in the X-ray projection technique. However, most of current 3D reconstruction methods are still not paying much attention to it. Therefore, one of the most important purposes of my research path in the future is focus on the estimation and compensation the motion of coronary artery. And this result could be applied as a pre-processing step on the rotational image sequence before put it into the reconstruction algorithm.

BIBLIOGRAPHY

- Andriotis A., Zifan A., Gavaises M. et al., "A new method of three-dimensional coronary artery reconstruction from X-ray angiography: validation against a virtual phantom and multislice computed tomography", *Catheterization and Cardiovascular Interventions*, vol. 71, no. 1, pp: 28–43, Jan. 2008.
- Anwar A., Xishi H., Jing R., "Endoscopy-MR Image Fusion for Image Guided Procedures", *International Journal of Biomedical Imaging*, Volume 2013, Article ID 472971, 2013.
- Cimen S., Hoogendoorn C. et al., "Reconstruction of Coronary Trees from 3DRA Using a 3D+t Statistical Cardiac Prior", *MICCAI 2014, Part II, LNCS 8674*, pp: 619–626, 2014.
- Cristiano B., Gonzalo T. et al., "Three-dimensional reconstruction of coronary arteries based on the integration of intravascular ultrasound and conventional angiography", *Revista Brasileira de Cardiologia Invasiva (English Edition)*, volume 23, pp: 134-138, April–June 2015.
- Feuillatre H., Sanokho B., Nunes J-C., Bedossa M., Toumoulin C., "Automatic determination of optimal view for the visualization of coronary lesions by rotational X-ray angiography", *IRBM*, pp: 291–295, 2013.
- Garcia J.A., Chen J., Hansgen A., et al., "Rotational angiography (RA) and three dimensional imaging (3-DRA): an available clinical tool", *Int J. Cardiovasc Imaging*, volume 23, pp: 9–13, 2007.
- Garcia JA, Movassaghi B, Casserly IP, Klein AJ, Chen SJ, Messenger JC, Hansgen A, Wink O, Groves BM, Carroll JD, "Determination of optimal viewing regions for X-ray coronary angiography based on a quantitative analysis of 3D reconstructed models", *Int J. Cardiovasc Imaging*, 25:455-462, 2009.
- Green N E et al., "Angiographic views used for percutaneous coronary interventions: a three dimensional analysis of physician-determined versus computer generated views Catheter", *Cardiovasc. Interv.*, volume 64, pp: 451–459, 2005.
- Heart disease and stroke statistics, A report from the American Heart Association Statistics Committee and Stroke Statistics Subcommittee, *Circulation* 2016.

- Hudson P.A., Klein A.J., Kim M.S., Wink O. et al., "A novel dual-axis rotational coronary angiography evaluation of coronary artery disease—case presentation and review", *Clin Cardiol*, volume 33, pp: 16-9, 2010.
- Jin Bae Lee, Sung Gug Chang, So Yeon Kim, Young Soo Lee, Jae Kean Ryu, Ji Yong Choi, Kee Sik Kim, Jae Sik Park, "Assessment of three dimensional quantitative coronary analysis by using rotational angiography for measurement of vessel length and diameter", *Int J Cardiovasc Imaging*, 28(7): 1627–1634, 2012.
- Kern M. L., "The Cardiac Catheterization Handbook", Elsevier Health Sciences, p. 416, 2011.
- Lv S., Meng C., Zhou F., Liu B., Zhou X., "Visual model based C-Arm system calibration and image correction", *International Conference on biomedical engineering and informatics*, pp: 1–5, China, 2009.
- Min Yang, Xu Han, Xiaojun Wu, Gang Zhao, Dongtao Wei, Tian Lang, Shunli Zhang, "Artifacts correction method for fan-beam CT with projections asymmetrically truncated on both sides", *NDT & E International*, Volume 87, pp: 24-30, April 2017.
- Minghua Li, Jiayin Zhang, Jingwei Pan, Zhigang Lu, "Coronary Stenosis: Morphologic Index Characterized by Using CT Angiography Correlates with Fractional Flow Reserve and Is Associated with Hemodynamic Status", *Radiological Society of North America*, Volume 269, Issue 3, 2013.
- Mufit Cetin, Ali Iskurt, "An Automatic 3-D Reconstruction of Coronary Arteries by Stereopsis", *J Med Syst*, pp: 40-94, 2016.
- Nassir Navab, Sandro-Michael Heining, Joerg Traub, "Camera Augmented Mobile C-Arm (CAMC): Calibration, Accuracy Study, and Clinical Applications", *IEEE Transactions on Medical Imaging*, vol. 29, no.7, pp: 1412-1423, 2010.
- Scarfe, William C., and Allan G. Farman, "What is Cone-Beam CT and How Does it Work?", *Dental Clinics of North America*, 52.4: 707-730, 2008.
- Sedentexct, "Technical Description of CBCT", www.sedentexct.eu, Accessed 20 August 2016.
- Segars W.P., Sturgeon G., Mendonca S., Grimes Jason, Tsui B.M.W., "4D XCAT phantom for multimodality imaging research", *Medical Physics*, vol. 37, issue 9, p. 4902, 2010.

- Taewoo Park, Seung Yeon Shin, Youngtaek Hong, Soochahn Lee, Hyuk-Jae Chang, Il Dong Yun, "Nonrigid 2D registration of fluoroscopic coronary artery image sequence with propagated deformation field", Proc. SPIE 10137, Medical Imaging 2017: Biomedical Applications in Molecular, Structural, and Functional Imaging, Florida, 2017.
- Wen Pei Liu, Yoshito Otake, Mahdi Azizian, Oliver J. Wagner, Jonathan M. Sorger, Mehran Armand, Russell H. Taylor, "2D–3D radiograph to cone-beam computed tomography (CBCT) registration for C-arm image-guided robotic surgery", *Int J Comput Assist Radiol Surg*, 10(8): 1239–1252, 2015.
- Yang J., Cong W., Chen Y., Fan J., Liu Y., Wang Y., "External force back-projective composition and globally deformable optimization for 3-D coronary artery reconstruction", *Phys Med Biol.*, volume 59, pp: 975-1003, 2014.
- Zeng, Gengsheng Lawrence. "Medical Image Reconstruction" Heidelberg: Springer (2010).
- Zhonghua Sun, "Coronary CT angiography with prospective ECG-triggering: an effective alternative to invasive coronary angiography", *Cardiovascular Diagnosis and Therapy*, vol 2, No 1, March 2012.